A FINITE DIFFERENCE SOLUTION TO THE TWO-DIMENSIONAL WALL JET ON A COMBUSTION TURBINE BLADF

by

Martin David Harsh III

Thesis submitted to the Graduate Faculty of the
Virginia Polytechnic Institute and State University
in partial fulfillment of the requirements for the degree of

MASTER OF SCIENCE

in

Mechanical Engineering

APPROVED:

Hal L. Moses, Chairman

Walter F. O'Brien

William C. Thomas

May 1978

Blacksburg, Virginia

Acknowledgments

The author would like to express his gratitude to fellow graduate students and faculty members in the College of Engineering with whom he had the honor to associate while studying at Virginia Polytechnic Institute and State University.

The author is indebted to of the Mechanical Engineering Department for the opportunities and experience gained as a teaching assistant.

A special thanks is extended to his parents,

and sisters,

Their support and encouragement is invaluable.

Table of Contents

Table of Contents (continued)

List of Figures

List of Figures (continued)

List of Tables

Nomenclature

A	van Driest damping factor in the inner-law, eddy-viscosity formulation
A_n, B_n, C_n, D_n	Coefficients in the finite-difference form of the boundary-layer momentum equation
a	Axial length of combustion turbine blade profile
b	y-intercept of the single-parabolic camberline equation
C_f	Skin friction coefficient
C_1, C_2, C_3, C_4	Intermediate quantities in the turbulent, two-layer velocity profile
c	Chord length
D	Intermediate quantity in the function governing the coordinate transformation
d	x coordinate of the vertex of the single-parabolic camberline equation
e	Napierian base
f	Function resulting from the similarity transformation of the boundary-layer momentum equation
G	The stretching function
H_{12}	Shape factor
K	Constant in the edge velocity equation for the laminar flow geometries
l	Camberline length
m	(i) Parameter governing the shape of the single-parabolic camberline, or (ii) pressure gradient parameter
N	Parameter controlling the amount of "stretching" in the coordinate transformation
P	(i) Pressure, or (ii) polynomial approximation to the wake function

	used in the turbulent, two-layer, velocity profile
Re_r	Reference Reynolds number
Re_x	Reynolds number based on x
Re_δ	Reynolds number based on δ
s	Blade pitch
u	x-component of velocity
u^+	Dimensionless x-component of velocity ($= \bar{u}\sqrt{\bar{\rho}/\bar{\tau}_\omega}$)
V_j	Wall-jet velocity at initial station
v	y-component of velocity
x	Streamwise coordinate
y	Transverse coordinate
y^+	Dimensionless transverse coordinate ($= \bar{y}\sqrt{\bar{\tau}_\omega/\bar{\rho}}/\bar{\nu}$)
α	Constant in stretching function -- from G'(0)
α_1	Inlet blade angle
α_2	Exit blade angle
β	Constant in stretching function -- from G(0)
δ	Boundary layer thickness
δ^*	Boundary-layer displacement thickness
δ^*_{inc}	Incompressible boundary-layer displacement thickness
ε	(i) Eddy viscosity, or (ii) tolerance on the gradient of the u-profile at the boundary-layer edge
ε_i	Inner eddy-viscosity formulation
ε_o	Outer eddy-viscosity formulation
η	(i) Normalized transverse distance, or (ii) similarity variable

η_s	Transverse distance at which turbulent velocity profiles switches from inner to outer formulation
θ	Boundary layer momentum thickness
μ	Absolute viscosity
ν	Kinematic viscosity
ρ	Density
σ	Total viscosity
τ	Shear stress
ϕ	Arbitrary function of x and y

Subscripts - Superscripts

$[\ ]_e$	Evaluated at the edge
$[\ ]^i$	From the i^{th} iteration
$[\ ]_\ell$	Evaluated in a linearized manner
$[\ ]_{m,n}$	Element (m,n) from the boundary-layer grid system
$[\ ]_r$	Reference value
$[\ ]_w$	Evaluated at the wall
$[\bar{}]$	Dimensional quantity
$[\tilde{}]$	Dimensionless quantity

1. Introduction

The objective of the present investigation is the development of a calculation technique capable of predicting boundary layer velocity profiles downstream from a tangentially oriented wall jet. The boundary layer calculation is applied to the steady, two-dimensional, incompressible, homogeneous flow over representative combustion turbine blade surfaces. The work has been conducted in coordination with the Turbomachinery Research Laboratory (TRL) at Virginia Polytechnic Institute and State University. The ultimate objective of this line of research is the determination of the film heat transfer coefficient for the compressible flow of combustion gases through turbine blade passages protected by film cooling.

A great deal of engineering effort has been spent in attempts to increase the thermal efficiency of the combustion turbine. A dual approach is currently being exercised with research being conducted on axial flow compressors to reduce the parasitic effect of compressor power consumption and on axial flow turbines to make more power available for useful work. The trend is toward higher turbine inlet temperatures on the downstream side of the machines. The American Society of Mechanical Engineers reports military engine requirements of alternate operation between 1400 C and 1900 C at the turbine inlet with high temperature technology being developed for operation in excess of 2200 C[1].* The effect of increasing the machine temperature

---

* Numbers in brackets designate References at end of paper.

ratio (the ratio of turbine inlet temperature to ambient temperature) is illustrated in Fig. 1. The approximate point of operation of the General Electric T64-6B combustion turbine used at the TRL compressor test facility is shown for comparison purposes.

The increased turbine inlet temperature will produce additional stresses in turbine blading already exposed to some of the most severe operating conditions imposed on machine elements. Centrifugal stresses, vibratory stresses, thermal stresses, corrosion, and erosion lead to early blade failure. The need for efficient blade cooling schemes becomes imperative with the move to higher turbine inlet temperatures.

Blade cooling schemes which have been considered include internal convection cooling (with a variety of fluids considered as the energy exchange medium) and film cooling. Included in the realm of film cooling is ablation, transpiration, and jet injection cooling. Ablation cooling consists of the evaporation of the surface material to produce an insulating layer of gases. The ablation method of surface protection has received little attention from turbine designers and has been used primarily with re-entry vehicles and rocket motors. Transpiration or "sweat" cooling involves the injection of gases through the protected surface. Porous metals and ceramics are being considered for use in combustion turbines. As yet, no porous materials possess the strength required to withstand the stresses imposed on turbine blading. Wall jet injection, either through discrete holes or continuous slots, has received the most attention from turbine designers. Goldstein [2] cites an investigation

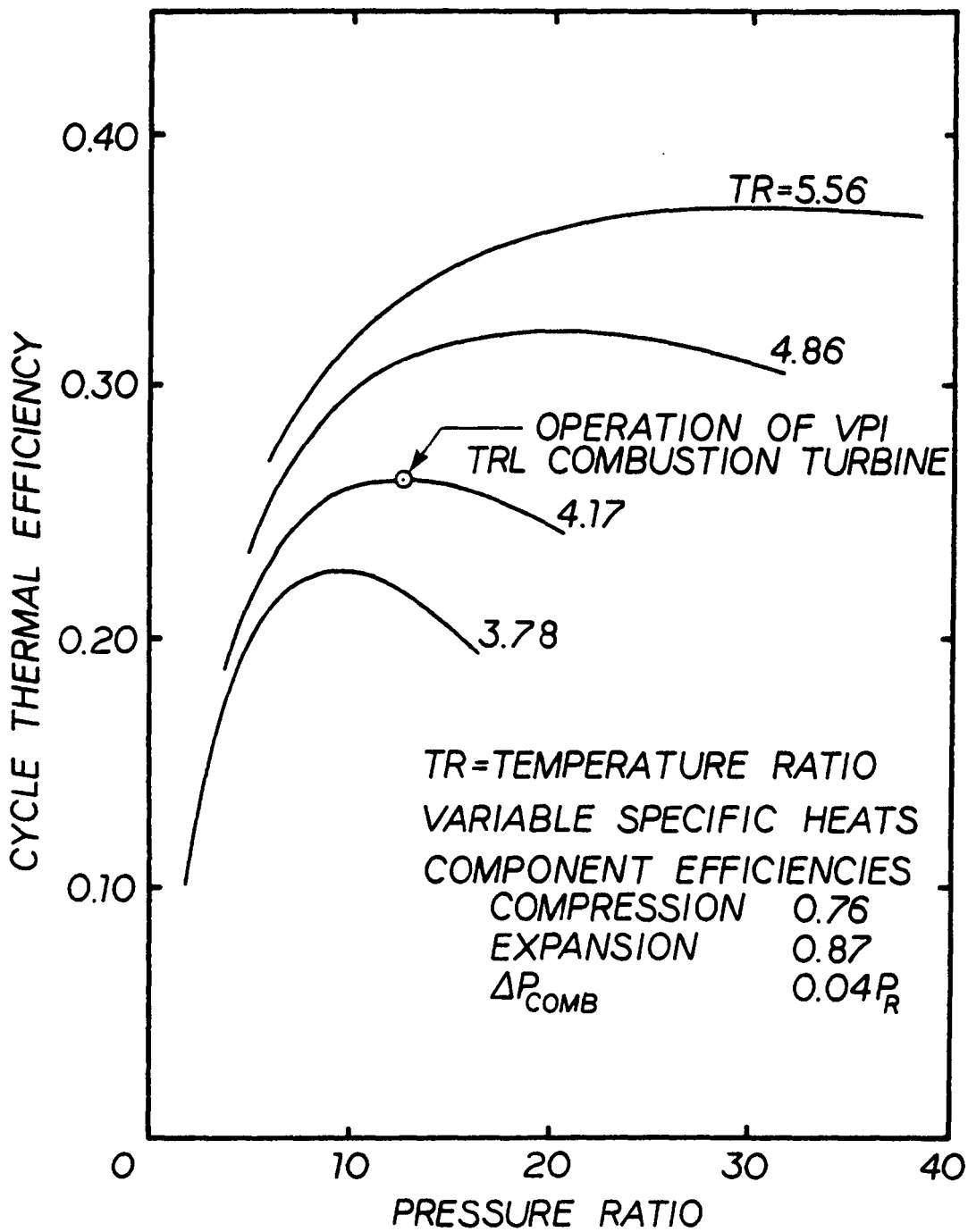

Fig. 1 Combustion Turbine Thermal Efficiency

by Eckert and Livingood in which the most efficient use of a unit of coolant was determined to be internal convection cooling with jet injection into the stream.

The reports of Goldstein [2], and Beckwith and Bushnell [3] serve as adequate literature reviews in the field of film cooling. Goldstein reports in detail the work of numerous investigators, concentrating on film cooling through wall jet injection. Various injection geometries and combinations of free-stream and injected stream fluids yielding non-homogeneous flows are presented. Beckwith and Bushnell deal with wall jet injection in supersonic flow. Their investigation is directed toward cooling re-entry and supersonic flight vehicles.

One of the earliest and perhaps most significant attempts at predicting wall jet behavior is by Glauert [4]. Glauert developed similarity solutions for laminar and turbulent wall jets spreading either radially or two-dimensionally over a surface. Glauert's study applies to wall jet flow with a zero velocity free stream.

McGahan [5] attacked the wall jet flowing in the presence of a zero velocity free stream and in the presence of an adverse pressure gradient. He used a five parameter integral analysis which required approximations for the shear stress at five locations in the boundary layer for the adverse pressure gradient case.

More exotic techniques by Beckwith and Bushnell [3], Miner [6], and Levine [7] attempt to calculate the behavior of the wall jet in supersonic, reacting flows.

The present investigation has been conducted in two parts. The first portion was spent developing a turbine vane profile representative of modern combustion turbines. The second, and most lengthy portion of the investigation dealt with the development of a finite difference calculation to predict the interaction of a wall jet with some initial boundary layer development which had occurred on the blade surfaces up to the point of injection. The calculation was verified by comparison of predicted results with results from well-known solutions for both laminar and turbulent boundary layer flows.

The following discussion begins with a description of the method used to generate the turbine vane profile. The boundary layer analysis follows. The equations governing conservation of mass and momentum in the boundary layer are adapted to the finite-difference grid used in the solutions. Included are descriptions of the boundary conditions, the eddy viscosity model used in the turbulent flow calculations, and the wall-jet model at the point of injection into the boundary layer.

2. Turbine Blade Geometry

The selection of efficient airfoil sections is important to aerodynamicists and combustion turbine designers. "Airfoil efficiency" is a function of many parameters where the specific application of the airfoil must be defined before the optimum airfoil shape can be selected. The blade shape of interest to turbine designers is one which will accept the flow at a given incidence angle and turn the flow through the required deflection angle with minimum frictional losses. Frictional losses in a blade channel include the effects of profile loss, annulus loss, secondary flow loss, and tip clearance loss. Turbine designers lump these effects into the overall blade loss coefficient [8].
The flow considered in this investigation is analogous to the flow through a two-dimensional cascade. Thus, the overall loss coefficient consists of profile losses only.

Airfoil sections are specified by describing a thickness form and a camber line form. The thickness form is a description of the blade surface height relative to a straight, or zero camber, mean blade line. The thickness form may or may not be symmetric about the mean blade line. The camber line form is a description of the deviation of the actual mean blade line from the zero camber mean blade line. Jacobs [9] states that the thickness form primarily dictates the structural characteristics of the blade while the camber line form controls the important aerodynamic characteristics of an airfoil section.

The thickness forms which are commonly used for turbine blading include the C4, T6, and NACA 0012 base profiles. The C4 base profile is of British origin while the T6 and NACA 0012 base profiles were developed in the American combustion turbine industry. The C4, T6, and NACA 0012 base profiles are given in Table 1 where the blade surface height is a function of the camber line length. All profiles listed are symmetric about the mean line.

Camber line forms are specified as single circular, double circular, single parabolic, or double parabolic arcs. The camber line form chosen as representative of turbine blading is the single parabolic arc described by

$$y = m(x-d)^2 + b \tag{2.1}$$

A general blade section is shown in Fig. 2. The parameters m, d, and b defining the parabolic camber line are calculated by specifying the blade inlet angle, the blade exit angle, and the blade pitch. The blade angles are used to determine the optimum pitch-cord ratio from cascade data reported by Cohen [8]. The optimum pitch-cord ratio for various blade angles is given in Table 2.

A simple analytic treatment of Eq. 2.1, applying the boundary conditions

$$\tan(\alpha_1) = -2md \tag{2.2}$$

$$\tan(-\alpha_2) = 2m(a-d) \tag{2.3}$$

Table 1. C4, T6, And NACA 0012 Airfoil Shapes [9, 10]

x/ℓ	y/ℓ		
	C4	T6	NACA 0012
0.0125	0.0165	0.0117	0.01894
0.0250	0.0227	0.0154	0.02615
0.0500	0.0308	0.0199	0.03555
0.0750	0.0362	0.0237	0.04200
0.1000	0.0402	0.0274	0.04683
0.1500	0.0455	0.0340	0.05345
0.2000	0.0483	0.0395	0.05738
0.3000	0.0500	0.0472	0.06002
0.4000	0.0489	0.0500	0.05803
0.5000	0.0457	0.0467	0.05294
0.6000	0.0405	0.0370	0.04563
0.7000	0.0337	0.0251	0.03664
0.8000	0.0254	0.0142	0.02623
0.9000	0.0160	0.0085	0.01448
0.9500	0.0106	0.0072	0.00807
Leading Edge Radius	0.012ℓ	0.012ℓ	0.0158ℓ
Trailing Edge Radius	0.006ℓ	0.006ℓ	--

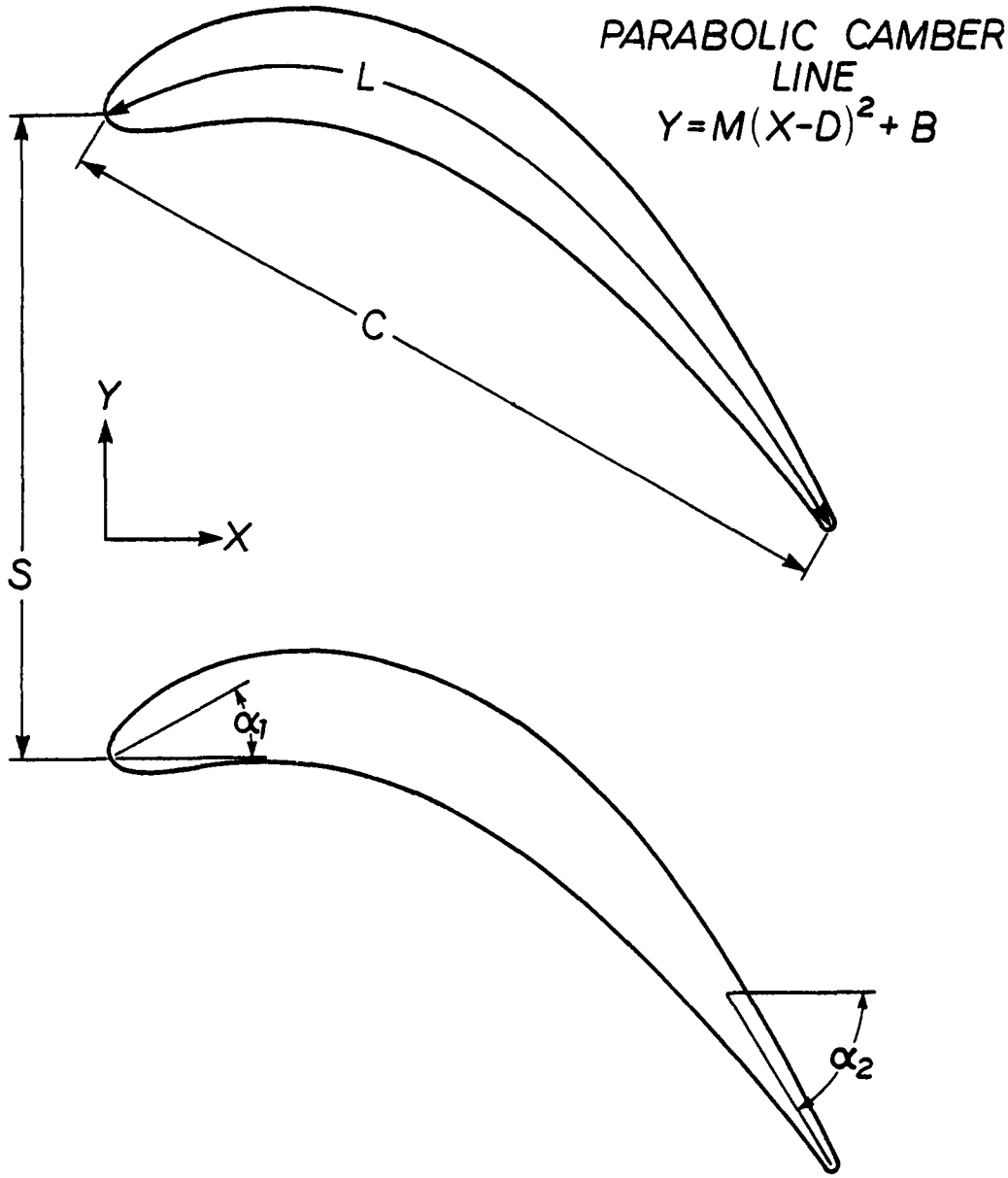

Fig. 2 General Cambered Airfoil Section

Table 2. Optimum Pitch-Cord Ratio, from Cohen [8]

Relative efflux Angle, degrees	Relative inlet gas angle, degrees				
	0	10	20	30	40
40	0.96	0.93	0.88	0.85	0.79
45	0.94	0.91	0.875	0.83	0.78
50	0.905	0.88	0.85	0.81	0.76
55	0.875	0.85	0.82	0.79	0.75
60	0.83	0.81	0.79	0.76	0.725
65	0.79	0.78	0.75	0.715	0.68
70	0.73	0.715	0.68	0.65	0.62

and the Pythagorean relation

$$a^2 + (md^2 + b)^2 = c^2 \tag{2.4}$$

yields the parameters controlling the shape of the parabolic camber line.

$$d = c \left\{ \left[1 - \frac{\tan(-\alpha_2)}{\tan(\alpha_1)} \right]^2 + \left[\frac{\tan^2(\alpha_1) - \tan^2(-\alpha_2)}{2\tan(\alpha_1)} \right]^2 \right\}^{-\frac{1}{2}} \tag{2.5}$$

$$m = \frac{-\tan(\alpha_1)}{2c} \left\{ \left[1 - \frac{\tan(-\alpha_2)}{\tan(\alpha_1)} \right]^2 + \left[\frac{\tan^2(\alpha_1) - \tan^2(-\alpha_2)}{2\tan(\alpha_1)} \right]^2 \right\}^{\frac{1}{2}} \tag{2.6}$$

$$b = \frac{c \cdot \tan^2(-\alpha_2)}{2\tan(\alpha_1)} \left\{ \left[1 - \frac{\tan(-\alpha_2)}{\tan(\alpha_1)} \right]^2 + \left[\frac{\tan^2(\alpha_1) - (\tan^2(-\alpha_2)}{2\tan(\alpha_1)} \right]^2 \right\}^{-\frac{1}{2}} \tag{2.7}$$

The camber line length is also required for the determination of the blade thickness. Substituting the parametric form of the parabolic camber line Eq. 2.1 into the equation for the length of a line in a plane

$$\ell = \int_{x_1}^{x_2} \sqrt{1+(dy/dx)^2}\, dx \tag{2.8}$$

the camber line length results.

$$\ell = m\left\{(x-d)\sqrt{(x-d)^2+(1/2m)^2} + (1/2m)^2 \ell n \left[(x-d)+\sqrt{(x-d)^2+(1/2m)^2}\right]\right\}\Bigg|_o^a \qquad (2.9)$$

The blade shape is constructed by distributing the thickness form over the camber line form described by Eq. 2.1 and Eq. 2.5-Eq. 2.7. A comparison of the three base profiles distributed over a parabolic camber line with $\alpha_1 = 0°$ and $\alpha_2 = 60°$ is shown in Fig. 3. The NACA 0012 thickness form distributed over the aforementioned camber line was selected as the representative turbine blade profile. This blade shape shows reasonable agreement with a first stage turbine vane from a large industrial combustion turbine reported by Dubberley [11]. A comparison of the cambered NACA 0012 section and the section reported by Dubberley is shown in Fig. 4.

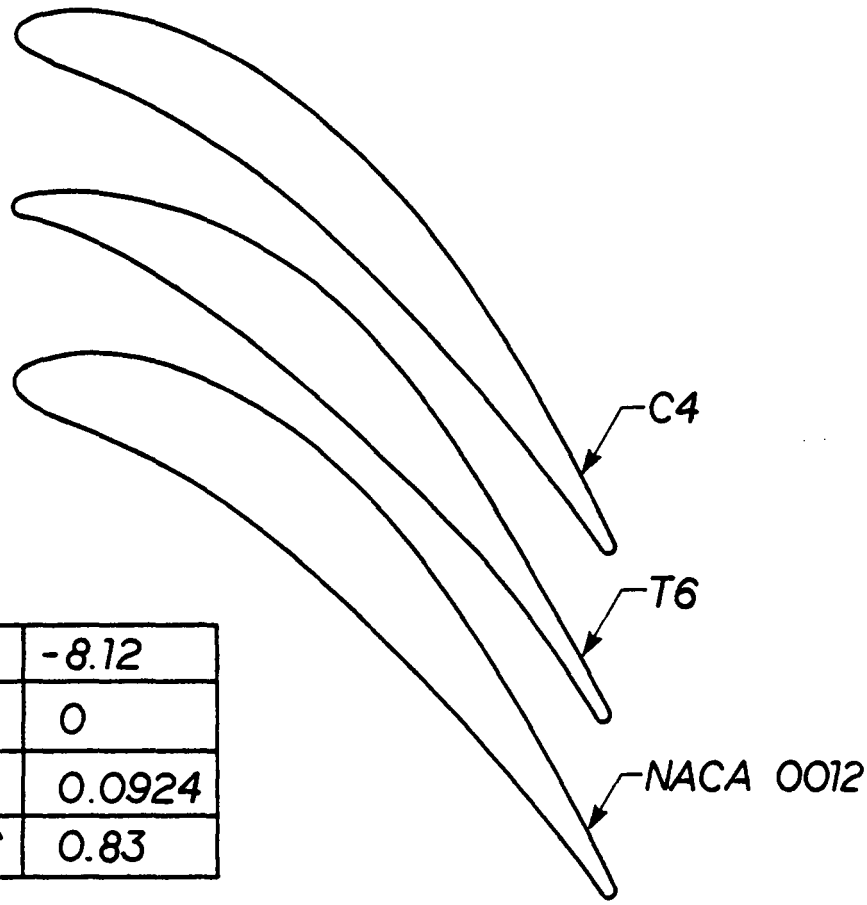

M	-8.12
D	0
B	0.0924
S/C	0.83

Fig. 3 C4, T6, and NACA 0012 Cambered Airfoil Sections with $\alpha_1 = 0^\circ$, $\alpha_2 = 60^\circ$

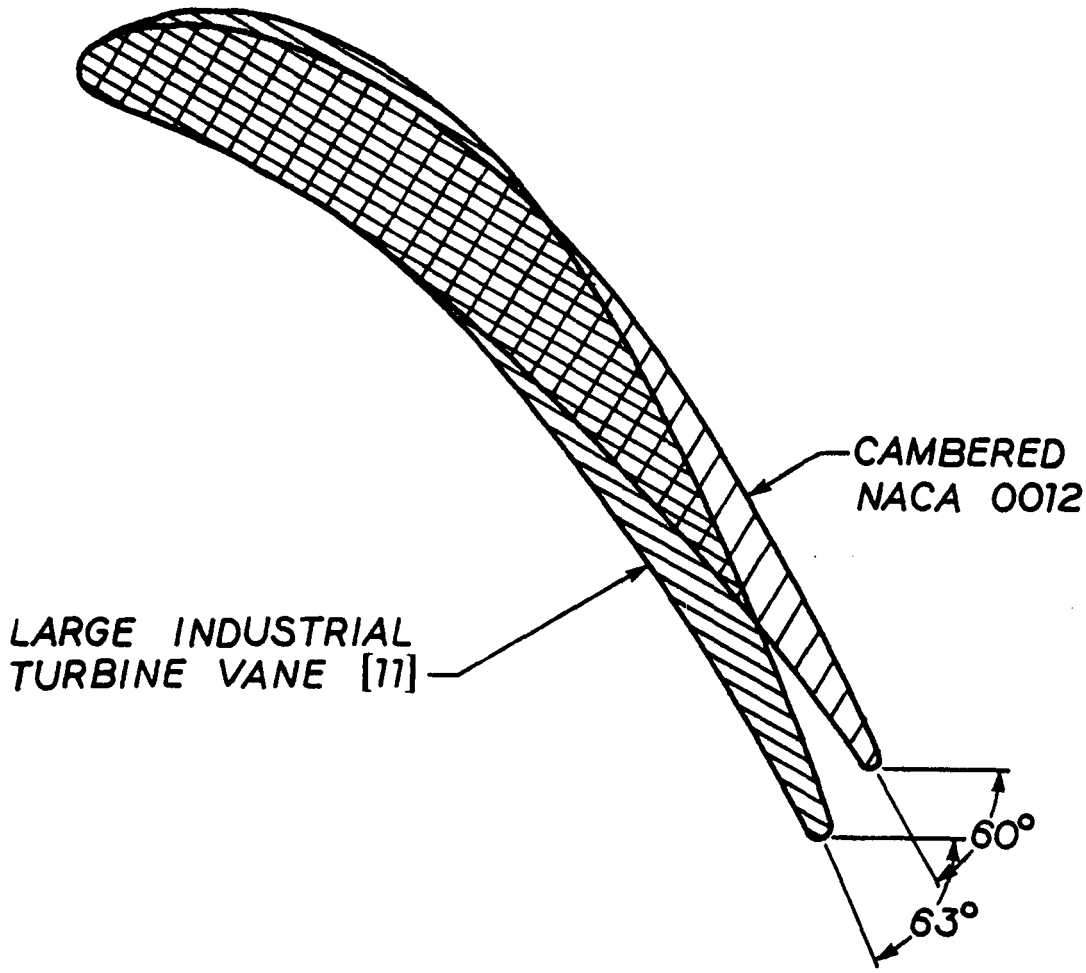

Fig. 4 Comparison of Cambered NACA 0012 Airfoil Section with Large Industrial Combustion Turbine Vane

3. Boundary Layer Analysis

The boundary layer analysis presented begins with the equations governing conservation of mass and momentum for steady, two-dimensional, homogeneous, incompressible, boundary-layer flow. Schlicting [12] presents the derivation of these equations along with the time averaging procedure and recognition of the Reynolds stresses. The governing equations are written explicitly for turbulent boundary-layer flow using the eddy viscosity concept to replace the Reynolds shear stress which results from the time averaging procedure. Simplification for laminar flow follows readily by setting the eddy viscosity equal to zero.

Temperature dependent fluid properties such as density and absolute viscosity are treated as variables. These properties remain as variables for ease in generalizing the analysis to include the effects of compressibility. The spatial derivatives of the temperature dependent fluid properties vanish for incompressible flow. The spatial derivative of the eddy viscosity term does not vanish for the incompressible case since the eddy viscosity is a property of the flow field and not the fluid itself.

3.1 The Governing Equations

Conservation of mass for two-dimensional flow is described by

$$\frac{\partial(\bar{\rho}\bar{u})}{\partial\bar{x}} + \frac{\partial(\bar{\rho}\bar{v})}{\partial\bar{y}} = 0. \tag{3.1}$$

Conservation of momentum for two-dimensional boundary-layer flow is expressed as

$$\bar{\rho}\bar{u}\frac{\partial \bar{u}}{\partial \bar{x}} + \bar{\rho}\bar{v}\frac{\partial \bar{u}}{\partial \bar{y}} = -\frac{d\bar{P}}{d\bar{x}} + \frac{\partial}{\partial \bar{y}}\left[(\bar{\mu} + \bar{\rho}\bar{\epsilon})\frac{\partial \bar{u}}{\partial \bar{y}}\right]. \tag{3.2}$$

It is convenient to non-dimensionalize Eq. 3.1 and Eq. 3.2. A coordinate transformation in the direction perpendicular to the wall is also useful for reasons which will be discussed later. The non-dimensionalizations and coordinate transformation utilized are those of Levine [7].

$$u = \frac{\bar{u}}{\bar{u}_r}$$

$$v = \frac{\bar{v}}{\bar{u}_r}$$

$$\rho = \frac{\bar{\rho}}{\bar{\rho}_r}$$

$$\mu = \frac{\bar{\mu}}{\bar{\mu}_r}$$

$$\epsilon = \frac{\bar{\epsilon}}{\bar{\nu}_r} = \frac{\bar{\epsilon}\bar{\rho}_r}{\bar{\mu}_r} \tag{3.3}$$

$$P = \frac{\bar{P}}{\frac{1}{2}\bar{\rho}_r\bar{u}_r^2}$$

$$x = \frac{\bar{x}}{\bar{L}_r}$$

$$y = G(\tilde{y})$$

where

$$\tilde{y} = \frac{\bar{y}}{\bar{L}_r}$$

and G is the "stretching" function governing the coordinate transformation in the direction perpendicular to the wall. Substitution of Eq. 3.3 into Eq. 3.1 and Eq. 3.2 yield, after some simplification,

$$\frac{\partial(\rho u)}{\partial x} + G' \frac{\partial(\rho v)}{\partial y} = 0 \tag{3.4}$$

$$\rho u \frac{\partial u}{\partial x} + G' \rho v \frac{\partial u}{\partial y} = - \frac{dP}{dx} + \frac{G'}{Re_r} \frac{\partial}{\partial y} [(\mu + \rho\varepsilon) G' \frac{\partial u}{\partial y}] \tag{3.5}$$

where

$$Re_r = \frac{\bar{\rho}_r \bar{u}_r \bar{L}_r}{\bar{\mu}_r} .$$

Defining the total viscosity σ,

$$\sigma \equiv \mu + \rho\varepsilon$$

and expanding the right-most term of Eq. 3.5, the equation describing conservation of momentum becomes

$$\rho u \frac{\partial u}{\partial x} + G' \rho v \frac{\partial u}{\partial y} = - \frac{dP}{dx} + \frac{G'}{Re_r} \left[\frac{\partial \sigma}{\partial y} G' \frac{\partial u}{\partial y} + \sigma \frac{G''}{G'} \frac{\partial u}{\partial y} + \sigma G' \frac{\partial^2 u}{\partial y^2} \right] . \tag{3.6}$$

3.2 Finite Difference Form of the Boundary Layer Equations

The finite difference technique utilized is an implicit method developed by Crank and Nicolson [13]. The unconditional stability of the Crank-Nicolson implicit finite difference technique has been demonstrated by Flugge-Lotz and Blotner [14] where finite difference stability is defined as the response of the technique to errors incurred by the finite difference approximations. A finite difference technique is termed stable if errors made in approximating the derivatives do not grow as the solution proceeds in the independent coordinate. Originally, the Crank-Nicolson technique was used to solve non-linear, parabolic partial differential equations of the heat conduction type. The technique has enjoyed considerable success in application to the boundary layer equations. The boundary layer mesh system used in the finite difference approximations is shown in Fig. 5.

The Crank-Nicolson finite difference approximations to the partial derivatives include:

$$\frac{\partial \phi}{\partial x} = \frac{\phi_{m+1,n} - \phi_{m,n}}{\Delta x} \tag{3.7}$$

$$\frac{\partial \phi}{\partial y} = \frac{1}{2}\left(\frac{\phi_{m,n+1} - \phi_{m,n-1}}{2\Delta y} + \frac{\phi_{m+1,n+1} - \phi_{m+1,n-1}}{2\Delta y}\right) \tag{3.8}$$

$$\frac{\partial^2 \phi}{\partial y^2} = \frac{1}{2}\left[\frac{\phi_{m,n+1} - 2\phi_{m,n} + \phi_{m,n-1}}{(\Delta y)^2} + \frac{\phi_{m+1,n+1} - 2\phi_{m+1,n} + \phi_{m+1,n-1}}{(\Delta y)^2}\right] \tag{3.9}$$

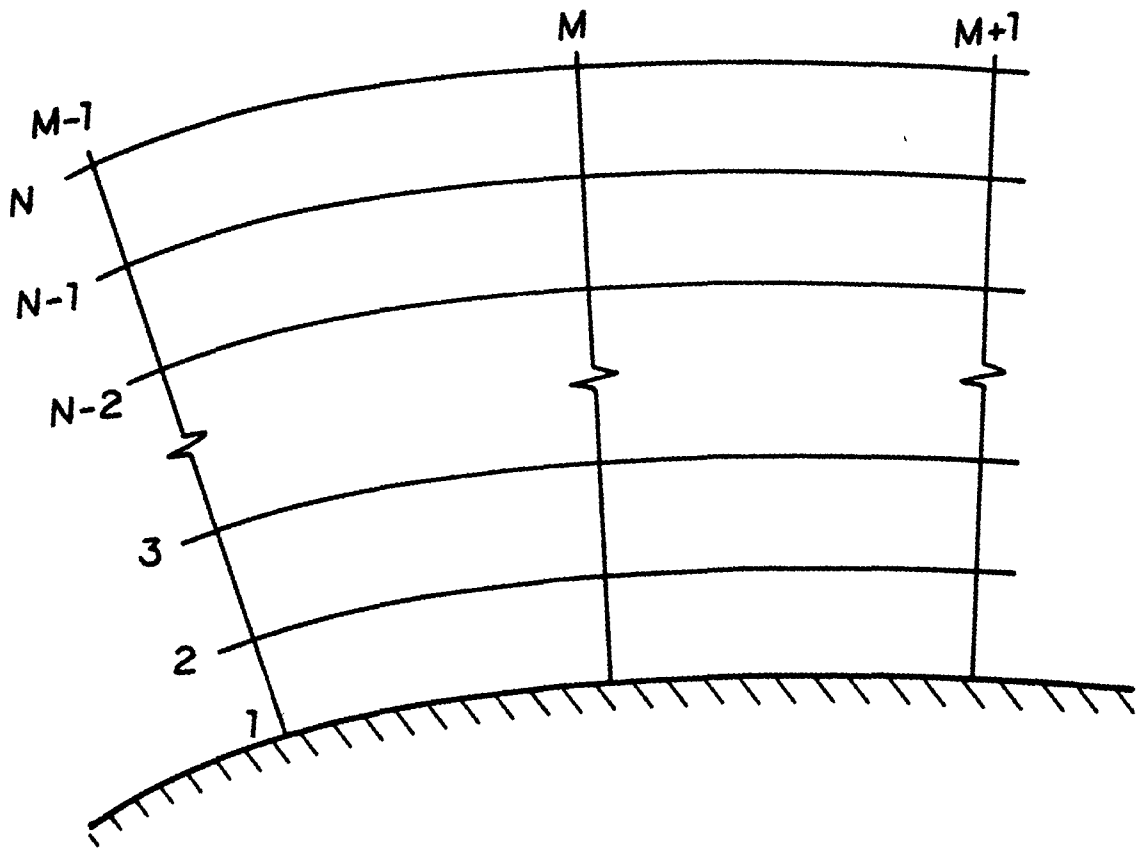

Fig. 5 Boundary Layer Grid System

where ϕ is some arbitrary function of x and y. Letting

$$\phi_y = \frac{\phi_{m,n+1} - \phi_{m,n-1}}{2\Delta y}$$

and

$$\phi_{yy} = \frac{\phi_{m,n+1} - 2\phi_{m,n} + \phi_{m,n-1}}{(\Delta y)^2}$$

Eq. 3.8 and Eq. 3.9 may be expressed in a somewhat more concise form.

$$\frac{\partial \phi}{\partial y} = \frac{1}{2}\left(\phi_y + \frac{\phi_{m+1,n+1} - \phi_{m+1,n-1}}{2\Delta y}\right) \tag{3.10}$$

$$\frac{\partial^2 \phi}{\partial y^2} = \frac{1}{2}\left[\phi_{yy} + \frac{\phi_{m+1,n+1} - 2\phi_{m+1,n} + \phi_{m+1,n-1}}{(\Delta y)^2}\right] \tag{3.11}$$

Replacing the arbitrary function ϕ by u in Eq. 3.7, Eq. 3.10, and Eq. 3.11, substituting these approximations into Eq. 3.6, and simplifying yields

$$A_n u_{m+1,n+1} + B_n u_{m+1,n} + C_n u_{m+1,n-1} = D_n \tag{3.12}$$

where the coefficients A_n, B_n, C_n, and D_n are given by

$$A_n = \frac{(\rho v)_\ell G'}{4\Delta y} - \frac{G'}{4Re_r \Delta y}\left[\frac{\partial \sigma}{\partial y} G' + \frac{\sigma G''}{G'}\right] - \frac{\sigma G'^2}{2Re_r (\Delta y)^2} \tag{3.13}$$

$$B_n = \frac{(\rho u)_\ell}{\Delta x} + \frac{\sigma G'^2}{(\Delta y)^2} \tag{3.14}$$

$$C_n = -\frac{(\rho v)_\ell G'}{4\Delta y} + \frac{G'}{4Re_r \Delta y}\left[\frac{\partial \sigma}{\partial y} G' + \frac{\sigma G''}{G'}\right] - \frac{\sigma G'^2}{2Re_r (\Delta y)^2} \tag{3.15}$$

$$D_n = \frac{(\rho u)_\ell u_{m,n}}{\Delta x} + \frac{u_y}{2}\left[\frac{G'^2}{Re_r}\cdot\frac{\partial\sigma}{\partial y} + \frac{\sigma G''}{Re_r} - (\rho v)_\ell G'\right] - \frac{dP}{dx} + \frac{\sigma G'^2 u_{yy}}{2Re_r} \quad . \tag{3.16}$$

The Crank-Nicolson finite difference approximations lead to the solution of the momentum equation about the point $(m+\frac{1}{2},n)$ as shown in Fig. 6. The momentum equation at each downstream location is represented by Eq. 3.12. Solution to the momentum equation at each downstream location is affected by solving the system of equations represented by Eq. 3.12. This system of equations constitutes a linear system of algebraic equations if the coefficients A_n through D_n are not functions of the u velocities at the downstream locations. The mass flux terms, ρu and ρv, and the total viscosity, σ, must therefore be linearized so that the system of equations may be solved. The solution of the momentum equation about the $m+\frac{1}{2}$ points lends itself readily to linearization. The mass flux terms and the total viscosity at the $m+\frac{1}{2}$ stations are thus approximated by

$$\phi^{(i+1)}_{m+\frac{1}{2},n} = \frac{1}{2}\left(\phi_{m,n} + \phi^{(i)}_{m+1,n}\right) \tag{3.17}$$

where the superscripts in the above equation imply an iterative process. The quantities at the (m+1)st station are first assumed equivalent to the quantities at the mth station. The system of equations represented by Eq. 3.12 is then solved to obtain a better estimate to the values at station m+1. The new estimates are then

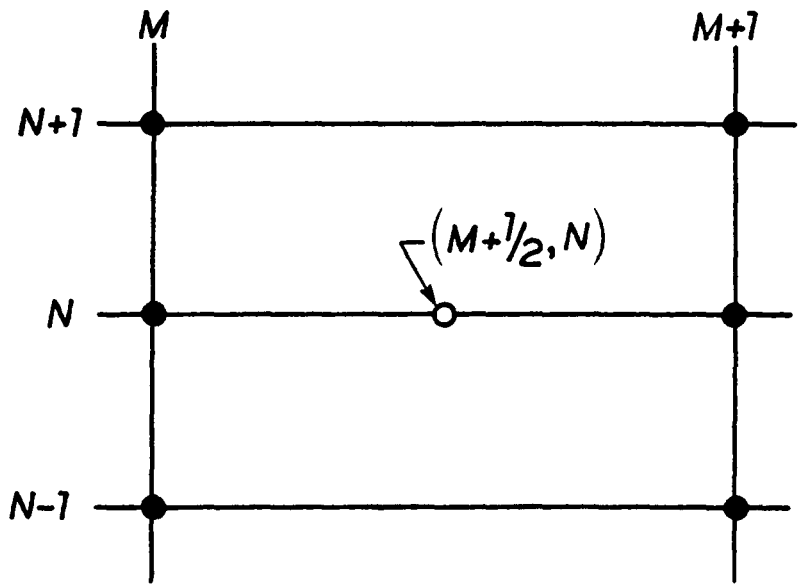

Fig. 6 Solution to the Momentum Equation

used in Eq. 3.17 as approximations to the values at m+1. The averaging process is repeated, the system of equations solved, and a new estimate to the values at m+1 obtained until the process converges. In general, it was assumed that the solution had converged when $u^{(i+1)}_{m+1,n}$ was within 1 per cent of $u^{(i)}_{m+1,n}$. A more strict convergence criteria, according to Clausing [15], is to bring the value of $v^{(i+1)}_{m+1,n}$ to within an acceptable tolerance of $v^{(i)}_{m+1,n}$.

The highly structured nature of the system of equations represented by Eq. 3.12 may be utilized in implementing the simultaneous solution technique. Inspection of Eq. 3.12 reveals that the coefficient matrix is tri-diagonal. The tri-diagonal system of equations contains n-2 equations in n-2 unknowns, u_2 through u_{n-1}. The extreme nodes, u_1 and u_n, are given by the edge conditions governing the boundary-layer flow.

The algorithm used to solve a tri-diagonal system of equations is one of forward elimination and back substitution. The first equation of the system, containing the three nodes nearest to the wall, is solved explicitly for the diagonal term. The sub-diagonal term of the first equation C_2u_1, is known from the boundary condition at the wall and may be incorporated into D_2. The result is substituted into the second equation for the sub-diagonal term. This equation is then solved explicitly for the diagonal term. The substitution process continues until the (n-2)nd equation of the system is solved explicitly for the diagonal term. The super-diagonal term, $A_{n-1}u_n$, is known from the boundary condition at the freestream

edge of the boundary layer and is incorporated into D_{n-1}. The substitution process is essentially one of forward elimination in which the sub-diagonal term of each equation is eliminated and the diagonal term is expressed in terms of the super-diagonal term and lesser coefficients. The result of the forward elimination procedure is an explicit expression for the (n-2)nd unknown in terms of the coefficients A_i through D_i, i = 2,3,4,...n-1. Once a value for the (n-2)nd unknown has been calculated, it may be back substituted into the expressions for the diagonal terms to obtain a complete solution to the system of equations.

The finite difference form of the equation governing conservation of mass, Eq. 3.4, is constructed for solution about the point shown in Fig. 7. The approximations to the partial derivatives in Eq. 3.4 are:

$$\frac{\partial \phi}{\partial x} = \frac{1}{2}\left(\frac{\phi_{m+1,n} - \phi_{m,n}}{\Delta x} + \frac{\phi_{m+1,n-1} - \phi_{m,n-1}}{\Delta x}\right) \tag{3.18}$$

$$\frac{\partial \phi}{\partial y} = \frac{\phi_{m+1,n} - \phi_{m+1,n-1}}{\Delta y} \, . \tag{3.19}$$

Pierce [16] argues that the finite difference approximation to $\partial\phi/\partial y$, Eq. 3.10, applied to the solution of the mass conservation equation leads to an unstable solution. Early in the analysis it was observed that for zero pressure gradient flow the approximation to $\partial(\rho v)/\partial y$ given by Eq. 3.10 produced negative y velocities -- a violation of the physics of the flow. Equation 3.19, recommended by Pierce, produced acceptable results for the zero pressure gradient case and

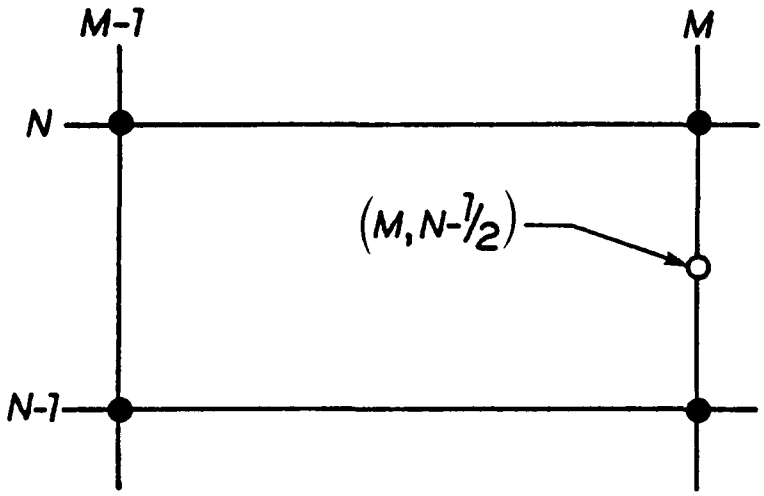

Fig. 7 Solution to the Equation Governing Conservation of Mass

was used in all subsequent solutions. Levine [7] used the approximation Eq. 3.10 but reported no y velocities. Substitution of Eq. 3.18 and Eq. 3.19 into Eq. 3.4, with simplifications, yields

$$(\rho v)_{m+1,n} = (\rho v)_{m+1,n-1} - \frac{\Delta y}{2G'_{n-\frac{1}{2}}} \left[\frac{(\rho u)_{m+1,n} - (\rho u)_{m,n}}{\Delta x} + \frac{(\rho u)_{m+1,n-1} - (\rho u)_{m,n-1}}{\Delta x} \right] \tag{3.20}$$

3.3 Boundary Conditions

The momentum equation for two-dimensional boundary-layer flow is a parabolic partial differential equation requiring closure on three sides. The fourth side, in the direction of the marching procedure, must remain open.

The usual no-slip condition was assumed for the conditions at the wall. The x velocity component at the wall is

$$\bar{u}(\bar{x},0) = 0.$$

The no-slip condition in terms of the discretized velocities of the finite difference grid is

$$u_{m,1} = 0. \tag{3.21}$$

An additional condition for the y velocity profile is required in order to solve Eq. 3.20. No mass injection was considered normal to the wall. Therefore,

$$\bar{v}(\bar{x},0) = 0.$$

In terms of the finite difference grid, the above becomes

$$v_{m,1} = 0. \tag{3.22}$$

Mass injection normal to the wall, as is the case with a porous surface, would imply some $v_{m,1} = v(x)$ and could be incorporated into the analysis.

Initial velocity profiles must be specified to start the calculation. Boundary layer calculations are typically started at the edge of the stagnation flow region. Most of the flow geometries investigated had no well defined stagnation region so alternate models for the initial profiles were used. The initial velocity profiles for both laminar and turbulent flow were assumed to be equivalent to those profiles which would develop on a flat plate in the same axial distance. The initial laminar profiles, for which a similarity analysis yields

$$\frac{\bar{\delta}}{\bar{x}} = \frac{5.0}{\sqrt{Re_x}} \tag{3.23}$$

were assumed to be

$$\frac{u}{u_e} = 2\eta - \eta^2 \tag{3.24}$$

and

$$\frac{v}{u_e} = \frac{2.6}{\sqrt{Re_x}} \left(\eta^2 - \frac{2}{3}\eta^3\right) \tag{3.25}$$

where:

$$\eta = \frac{\bar{y}}{\bar{\delta}} \tag{3.26}$$

$$Re_x = \frac{\bar{u}_e \bar{x}}{\bar{\nu}} \tag{3.27}$$

Moses' two parameter, two layer u profile [17] was used to start the turbulent flow calculations. Moses' profile is given by:

Viscous sublayer; $0 < \eta < \eta_s$

$$\frac{u}{u_e} = C_1\left(\frac{\eta}{\eta_s}\right) + C_2\left(\frac{\eta}{\eta_s}\right)^2 - C_4\, P(\eta)$$

$$\eta_s = \frac{52.7}{C_3 Re_\delta}$$

$$P(\eta) = 3\eta^2 - 2\eta^3$$

$$Re_\delta = \frac{\bar{u}_e \bar{\delta}}{\bar{\nu}} \tag{3.28}$$

$$C_1 = 8.86\, C_3$$

$$C_2 = 03.73\, C_3$$

$$C_3 = \frac{1}{0.41}\sqrt{\frac{C_f}{2}}$$

$$C_4 = C_3[\ell n(C_3 Re_\delta) + 1.1584] - 1$$

Outer layer; $\eta_s \leq \eta \leq 1$

$$\frac{u}{u_e} = 1 + C_3\, \ell n(\eta) + C_4[1 - P(\eta)].$$

A one-fifth power law analysis for turbulent, zero pressure gradient, boundary layer flow yields:

$$\frac{\bar{\delta}}{\bar{x}} = \frac{0.37}{Re_x^{0.2}} \tag{3.29}$$

$$C_f = \frac{0.0592}{Re_x^{0.2}} \quad . \tag{3.30}$$

The initial u profiles were specified by inputing the boundary layer thickness at the initial station, given by Eq. 3.29, and the parameter C_3. The skin friction coefficient in Eq. 3.28 was evaluated using Eq. 3.30. The initial v profile was obtained from the power law analysis and is

$$\frac{v}{u_e} = \frac{0.0501\eta^{1.2}}{Re_x^{0.2}} \tag{3.31}$$

The third boundary condition required is a description of the free-stream velocity at the edge of the boundary layer. The edge condition is derived from a potential flow analysis about the geometry of concern. The edge condition in laminar flow for the various classic geometries investigated is given by the general equation

$$\bar{u}_e(\bar{x}) = K\bar{x}^{\bar{m}} \quad . \tag{3.32}$$

The edge condition for the turbulent boundary layer calculations in the cascade channel was obtained from a potential flow solution by

Katsanis [18]. A summary of the boundary layer edge conditions is given in Table 3.

It is impractical to supply a discrete edge condition for each downstream location due to the large number of finite difference steps needed to proceed in the downstream direction. A method of interpolation was sought which would adequately describe the edge velocity and edge velocity gradient using a minimum number of data points. The edge velocity and edge velocity gradient are used in the Bernoulli relation

$$\frac{dP}{dx} = -\rho_e u_e \frac{du_e}{dx} \tag{3.33}$$

to determine the pressure gradient driving the boundary layer flow. Cubic spline interpolation using the "free end" condition was chosen as the interpolation technique. This method has a significant advantage over nth order polynomial interpolation. The derivative of the cubic spline interpolating polynomial may be used to describe the edge velocity gradient. No finite difference technique is required to calculate the pressure gradient. Ahlberg [19] discusses the utility of the cubic spline as an approximation technique.

One additional boundary condition is required to control the boundary layer thickness and the number of mesh nodes in the y direction. The criterion for the u velocity gradient at the boundary layer edge is

$$\frac{\partial \bar{u}}{\partial \bar{y}} = 0.$$

Table 3. Boundary Layer Edge Conditions

Geometry	Freestream edge velocity	From
Laminar, flat plate	$\bar{u}_e$ = constant	Potential flow theory
Laminar, 27° wedge	$\bar{u}_e$ = constant · $\bar{x}^{0.17647}$	Potential flow theory
Laminar, 16.2° expansion corner	$\bar{u}_e$ = constant · $\bar{x}^{-0.082569}$	Potential flow theory
Turbulent, flat plate	$\bar{u}_e$ = constant	Potential flow theory
Turbulent, cascade channel	--	Potential flow solution by Katsanis [18]

The above condition in terms of the finite difference grid becomes

$$\frac{1}{u_e} \cdot \frac{u_{m,n} - u_{m,n-1}}{\Delta y} \leq \varepsilon \qquad (3.34)$$

where the tolerance ε is given by the u profile at the initial station. A mesh point is added and the solution at the mth station repeated until the tolerance is met. The coarse nature of the grid required to start several of the calculations necessitated the specification of the edge tolerance by some means other than Eq. 3.34 applied to the initial velocity distribution. In these cases, the edge tolerance was chosen sufficiently small so that the calculation carried along several extra nodes essentially outside the boundary layer.

3.4 The Coordinate Transformation

A coordinate transformation proves useful in allowing the solution technique to "see" the high velocity gradient near the wall characteristic of turbulent flow. Pierce [16] uses a simple technique where the boundary layer thickness is represented by a geometric series. Small steps are taken across the viscous sublayer with the step size becoming increasingly larger across the turbulent core. Pierce's method has the disadvantage of a complicated set of finite difference equations. Cebeci [20] uses a combination Mangler-Levy-Lees transformation stretching the boundary layer in both the x and

y directions. Cebeci's method results in a solution plane which has a near constant boundary layer thickness with compressibility effects greatly reduced. The coordinate transformation used here is identical to that of Levine [7] which stretches the physical plane near the wall. The finite difference solution to the equations is conducted in the transformed plane with constant step sizes in both the x and y direction. The stretching function is given by

$$y = G(\tilde{y}) = \tilde{\delta}_i \left\{ \ell n \left[(e-1)\left(\frac{\tilde{y}}{\tilde{\delta}_i} + \alpha\right) + 1 \right] \right\}^{1/N} - \tilde{\delta}_i \beta \quad (3.35)$$

where α and β are constants determined from the conditions on G(0) and G'(0). The amount of stretching is controlled by the exponent N. The first and second derivatives of the stretching function are also required. Defining the intermediate quantity D,

$$D \equiv (e-1)\left(\frac{\tilde{y}}{\tilde{\delta}_i} + \alpha\right) + 1 \quad (3.36)$$

G' and G'' may be written:

$$G' = \frac{(e-1)}{ND} (\ell nD)^{\frac{1}{N} - 1} \quad (3.37)$$

$$G'' = \frac{1}{N\tilde{\delta}_i} \left(\frac{e-1}{D}\right)^2 \left[\left(\frac{1}{N} - 1\right) (\ell nD)^{\frac{1}{N} - 2} - (\ell nD)^{\frac{1}{N} - 1} \right] . \quad (3.38)$$

The inverse stretching function is given by

$$\tilde{y} = \tilde{\delta}_i \left\{ \frac{1}{e-1} \left[\exp\left(\left(\frac{y}{\tilde{\delta}_i} + \beta \right)^N \right) - 1 \right] - \alpha \right\} \quad . \tag{3.39}$$

Values of α and β for various $G'(0)$ with $G(0) = 0$ are presented in Table 4.

The coordinate transformation is applied only to turbulent flow calculations. Numerical difficulties arose when stretching the y coordinate in laminar flow as a result of the extremely small velocities near the wall. The equations for laminar flow are simplified by substituting:

$$y = G(\tilde{y}) = \tilde{y} \tag{3.40}$$

$$G'(\tilde{y}) = 1 \tag{3.41}$$

$$G''(\tilde{y}) = 0 \quad . \tag{3.42}$$

3.5 The Eddy Viscosity Model

The eddy viscosity concept is used to replace the Reynolds shear stress in the time averaged momentum equation. A two-layer eddy viscosity model developed by Cebeci [20] is incorporated into the calculation technique. Cebeci's turbulent viscosity model consists of the van Driest inner law and Clauser outer law, modified to include the effects of compressibility, pressure gradient, and mass injection normal to the wall. Cebeci's model as given below is in simplified form neglecting mass injection normal to the wall.

Inner law;

Table 4. Constants in the Stretching Function with G(0) = 0

G'(0)	10		100		1000		10,000	
N	$\alpha \cdot 10^3$	$\beta \cdot 10^2$	$\alpha \cdot 10^5$	$\beta \cdot 10^3$	$\alpha \cdot 10^7$	$\beta \cdot 10^4$	$\alpha \cdot 10^9$	$\beta \cdot 10^5$
2	4.249094	8.529137	4.295229	8.590775	4.295700	8.591403	4.295705	8.591409
3	7.871078	23.77220	25.21606	75.66456	79.77363	239.3225	25.22697	756.8093
4	8.648683	34.85052	40.61617	162.5214	188.6281	754.5247	875.5567	3502.229
5	8.517893	42.89963	48.39387	242.0699	272.2989	1361.526	1531.300	7656.509

$$\bar{\varepsilon}_i = 0.16\,\bar{y}^2 \left| \frac{\partial \bar{u}}{\partial \bar{y}} \right| \left[1 - \exp\left(-\frac{\bar{y}}{\bar{A}}\right)\right]^2 \tag{3.43}$$

$$\bar{A} = 26\,\bar{\mu} \left\{ \bar{\tau}_\omega \bar{\rho} \left[1 + 11.8 \frac{d\bar{P}}{d\bar{x}} \left(\bar{\rho}_\omega \bar{\mu}_\omega \left. \frac{\partial \bar{u}}{\partial \bar{y}} \right|_\omega^3 \right)^{-\frac{1}{2}} \right] \right\}^{-\frac{1}{2}} \tag{3.44}$$

Outer law;

$$\bar{\varepsilon}_o = 0.0168\,\bar{u}_e\,\bar{\delta}^*_{inc} \left[1 + 5.5 \left(\frac{\bar{y}}{\bar{\delta}} \right)^6 \right]^{-1} \tag{3.45}$$

$$\bar{\delta}^*_{inc} = \int_0^{\bar{\delta}} \left(1 - \frac{\bar{u}}{\bar{u}_e} \right) d\bar{y} \tag{3.46}$$

Applying the dimensionless relations and coordinate transformation given by Eq. 3.3 to the eddy viscosity model above yields:

Inner law;

$$\varepsilon_i = 0.16\,Re_r G'\tilde{y}^2 \left| \frac{\partial u}{\partial y} \right| \left[1 - \exp\left(-\frac{\tilde{y}}{A} \right) \right]^2 \tag{3.47}$$

$$A = 26\mu \left\{ Re_r\,\rho\mu_\omega \cdot \left. \frac{\partial u}{\partial \tilde{y}} \right|_\omega \left[1 + 11.8 \frac{dP}{dx} \left(\frac{Re_r}{\rho_\omega \mu_\omega \left. \frac{\partial u}{\partial \tilde{y}} \right|_\omega^3} \right)^{\frac{1}{2}} \right] \right\}^{-\frac{1}{2}} \tag{3.48}$$

Outer law;

$$\varepsilon_o = 0.0168\,Re_r u_e \delta^*_{inc} \left[1 + 5.5 \left(\frac{\tilde{y}}{\tilde{\delta}} \right)^6 \right]^{-1} \tag{3.49}$$

$$\delta^*_{inc} = \int_0^{\tilde{\delta}} \left(1 - \frac{u}{u_e}\right) d\tilde{y} \tag{3.50}$$

The eddy viscosity model was applied to the finite difference grid by calculating the turbulent viscosity at each node by both Eq. 3.47 and Eq. 3.49. The inner law was used to determine the turbulent viscosity until the value given by Eq. 3.47 exceeded that given by Eq. 3.49. The outer law was used once this intersection had been determined. The final turbulent viscosity distribution was obtained by averaging the turbulent viscosity at a given node with the four surrounding values at the same downstream location.

3.6 Boundary Layer Characteristics

The following boundary layer characteristics were calculated at each downstream location:

(i) displacement thickness, $\bar{\delta}^*$

$$\bar{\delta}^* = \int_0^{\bar{\delta}} \left(1 - \frac{\bar{\rho}\bar{u}}{\bar{\rho}_e \bar{u}_e}\right) d\bar{y} \tag{3.51}$$

(ii) momentum thickness, $\bar{\theta}$

$$\bar{\theta} = \int_0^{\bar{\delta}} \frac{\bar{\rho}\bar{u}}{\bar{\rho}_e \bar{u}_e} \left(1 - \frac{\bar{u}}{\bar{u}_e}\right) d\bar{y} \tag{3.52}$$

(iii) shape factor, H_{12}

$$H_{12} = \frac{\bar{\delta}^*}{\bar{\theta}} \tag{3.53}$$

(iv) skin friction coefficient, C_f

$$C_f = \frac{\bar{\tau}_\omega}{\frac{1}{2}\bar{\rho}_e \bar{u}_e^2} \tag{3.54}$$

The integrations above were performed using the trapezoidal method in the dimensionless plane. The wall shear stress for a Newtonian fluid is given by

$$\bar{\tau}_\omega = \bar{\mu}_\omega \left.\frac{\partial \bar{u}}{\partial \bar{y}}\right|_\omega \tag{3.55}$$

The velocity gradient in the y direction evaluated at the wall was calculated using a technique suggested by Clausing [15]. Clausing approximates the gradient at the wall with the arithmetic average of a linear approximation and a parabolic approximation given by

$$\left.\frac{\partial u}{\partial y}\right|_\omega = \frac{1}{\Delta y}\left(\frac{3}{16} u_{m,4} - \frac{17}{16} u_{m,3} + \frac{41}{16} u_{m,2} - \frac{27}{16} u_{m,1}\right) . \tag{3.56}$$

The above finite difference relation is written for discrete points in the dimensionless, stretched plane. Applying the no-slip condition at the wall, the velocity gradient in the physical plane may be written

$$\left.\frac{\partial \bar{u}}{\partial \bar{y}}\right|_\omega = \frac{\bar{u}_r G'(0)}{\bar{L}_r}\left(\frac{3}{16} u_{m,4} - \frac{17}{16} u_{m,3} + \frac{41}{16} u_{m,2}\right) . \tag{3.57}$$

Clausing's technique for evaluating derivatives at the wall was used in both the determination of the skin friction coefficient and the

evaluation of the eddy viscosity model, Eq. 3.48.

3.7 The Algorithm for Solution to the Governing Equations

The solution to the equations governing the boundary-layer flow was conducted on an electronic digital computer according to the algorithm below. The iterative process resulting from the linearization of the momentum equation was performed a minimum of three times for each downstream step. The solution for the downstream location was considered complete when successive u profiles at the downstream location had converged to within one per cent.

Crank-Nicolson algorithm

(i) Project the values at station m forward to station m+1.

(ii) Perform the linearizations required for the solution of the momentum equation.

(iii) Solve the momentum equation given by the system of tri-diagonal algebraic equations.

(iv) Check the edge condition given by Eq. 3.34. Add a mesh point and return to step (iii) if necessary.

(v) Solve the equation of conservation of mass.

(vi) Check for convergence of the u velocity profile. Return to step (ii) using the calculated values in the linearization scheme

if necessary.

(vii) Finalize the step downstream by calculating the boundary layer characteristics.

The code exists in two forms, one for laminar boundary layer calculations and a second for the turbulent counterpart. No capability exists in either code for transition from laminar to turbulent flow. The codes are constructed using functional blocks, or subroutines, to carry out the algorithm. The Appendix contains a flow diagram showing calls to and operations performed by the various functional blocks. The use of functional blocks should enable a later user to investigate the feasibility of other stretching functions, eddy viscosity models, etc.. Major differences between the laminar and turbulent codes exist in the subroutines controlling the stretching function, the eddy viscosity model, and the initial velocity profiles. For the laminar case, the stretching function is replaced by Eq. 3.40-Eq. 3.42, the eddy viscosity is "turned off" with $\bar{\epsilon} = 0$, and the initial velocity profiles are given by Eq. 3.24 and Eq. 3.25. Both codes contain temperature dependent fluid properties in array form so that compressibility effects may be incorporated into the analysis.

3.8 The Wall-Jet Model

The assumed form of the injected velocity profiles consists of some initial boundary layer development standing over a block or slug flow approximation for the flow issuing from the wall jet. The

injection geometry and wall jet model are shown in Fig. 8. The assumptions pertinent to the wall jet boundary layer analysis are:

(i) two-dimensional flow

(ii) steady flow

(iii) incompressible flow

(iv) homogeneous fluid

(v) negligible lip thickness

(vi) uniform static pressure across the injection point

The ratios δ_i/s and u_e/V_j govern the shape of the injected profiles.

The velocity distribution at the injection point is given in a piecewise manner using the previously defined laminar or turbulent velocity profiles to describe the initial boundary layer development (Eq. 3.24 and Eq. 3.25, or Eq. 3.28 and Eq. 3.31) and the slug flow approximation:

$$\left.\begin{aligned} \bar{u} &= V_j \\ \bar{v} &= 0 \end{aligned}\right\} \quad 0 < y < s \tag{3.58}$$

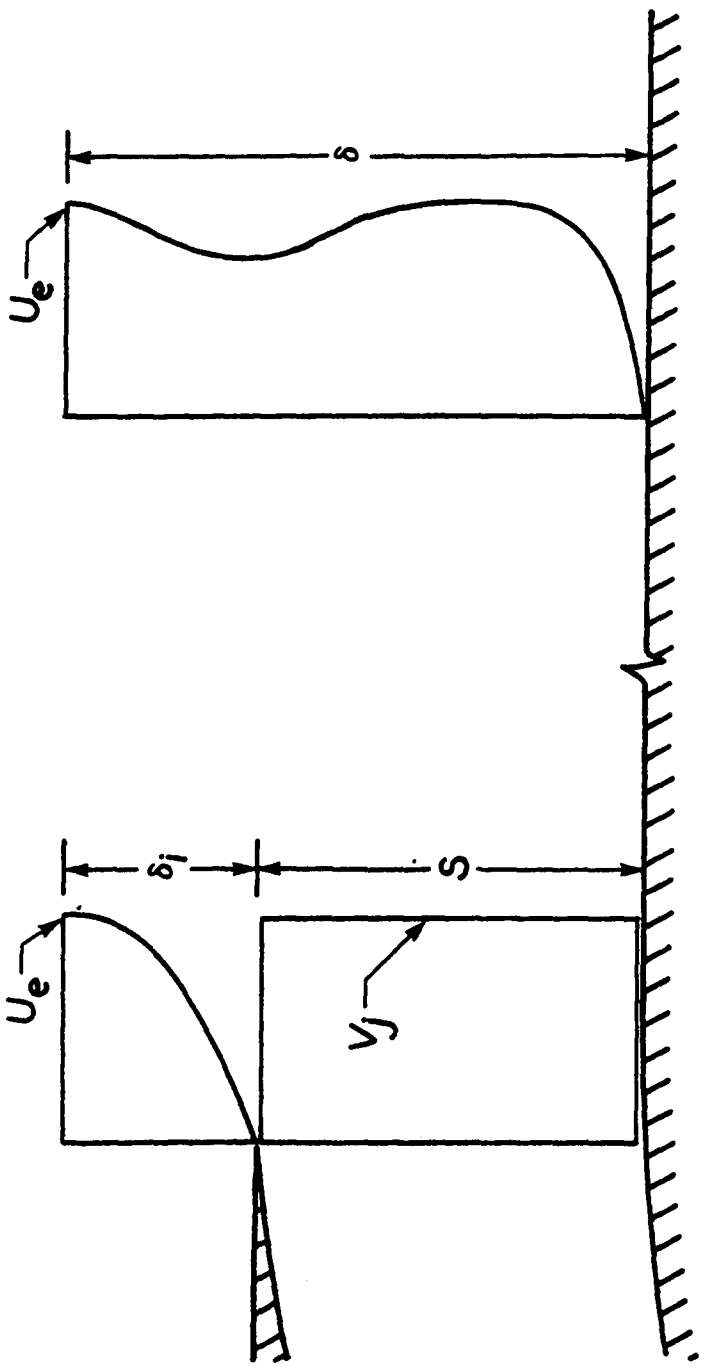

Fig. 8 Wall-Jet Model

4. Results

Several boundary layer flows were investigated to test the validity of the Crank-Nicolson algorithm as employed in the investigation. Three laminar boundary layer flows subjected to various pressure gradients along with turbulent, zero pressure gradient flow were considered. The boundary layer flow over the airfoil section was then calculated and compared with a second solution technique. Finally, the boundary layer flow with wall jet injection was calculated. The interaction of the wall jet with the initial boundary layer for zero pressure gradient flow and the flow over the airfoil section was considered.

4.1 Laminar Boundary Layer Calculations

Laminar boundary layer calculations were performed for the flow over three geometries: a flat plate with zero pressure gradient, a 27° half-angle wedge with negative (favorable) pressure gradient, and a 16.2° expansion corner with positive (adverse) pressure gradient. These three cases were investigated to test the response of the procedure to various pressure gradients. The solutions to the boundary layer flow over these geometries are well known and members of a large family of solutions known as the Falkner-Skan wedge flows. The Falkner-Skan solutions are similarity solutions where

$$\eta \equiv \bar{y} \left[\frac{m+1}{2} \cdot \frac{u_e}{\bar{\nu} x} \right]^{\frac{1}{2}} \tag{4.1}$$

$$f'(\eta) = \frac{u}{u_e} \tag{4.2}$$

and m is a parameter controlling the pressure gradient -- identical to the quantity m in Eq. 3.32. Substituting Eq. 4.1 and Eq. 4.2 into Eq. 3.2 with $\bar{\varepsilon} = 0$ there results

$$\frac{d^3f}{d\eta^3} + f \cdot \frac{d^2f}{d\eta^2} + \frac{2m}{m+1}\left[1 + \left(\frac{df}{d\eta}\right)^2\right] = 0 \tag{4.3}$$

subject to the boundary conditions

$$f(0) = \frac{df}{d\eta}(0) = 0 \tag{4.4}$$

$$\frac{df}{d\eta}(\infty) = 1 \tag{4.5}$$

The solution to Eq. 4.3 may be changed to an initial value problem if the value of $d^2f/d\eta^2$(@ η=0) can be selected to satisfy the asymptotic condition Eq. 4.5. White [21] has solved Eq. 4.3 and lists values of $d^2f/d\eta^2$(@ η=0) which satisfy the asymptotic condition for various values of the parameter m. For the three geometries above:

(i) flat plate; $d^2f/d\eta^2$(@ η=0) = 0.46960

(ii) 27° half-angle wedge; $d^2f/d\eta^2$(@ η=0) = 0.77476

(iii) 16.2° expansion corner; $d^2f/d\eta^2$(@ η=0) = 0.12864

Equation 4.3 was integrated numerically using IBM's Continuous System Modeling Program (CSMP) with the values for the initial conditions above. The boundary layer parameters given by Eq. 3.51-Eq. 3.54 were included in the CSMP calculation. The resulting boundary layer characteristics are:

(i) flat plate;

$$\frac{\theta}{x} = \frac{0.664}{\sqrt{Re_x}} \tag{4.6}$$

$$H_{12} = 2.59 \tag{4.7}$$

$$C_f = \frac{0.664}{\sqrt{Re_x}} \tag{4.8}$$

(ii) 27° half-angle wedge;

$$\frac{\theta}{x} = \frac{0.503}{\sqrt{Re_x}} \tag{4.9}$$

$$H_{12} = 2.37 \tag{4.10}$$

$$C_f = \frac{1.19}{\sqrt{Re_x}} \tag{4.11}$$

(iii) 16.2° expansion corner

$$\frac{\theta}{x} = \frac{0.838}{\sqrt{Re_x}} \tag{4.12}$$

$$H_{12} = 3.29 \tag{4.13}$$

$$C_f = \frac{0.174}{\sqrt{Re_x}} \tag{4.14}$$

The results from the Crank-Nicolson algorithm for the three geometries are shown in Fig. 9 - Fig. 15. The predictions from the Crank-Nicolson algorithm agree well with the Falkner-Skan similarity

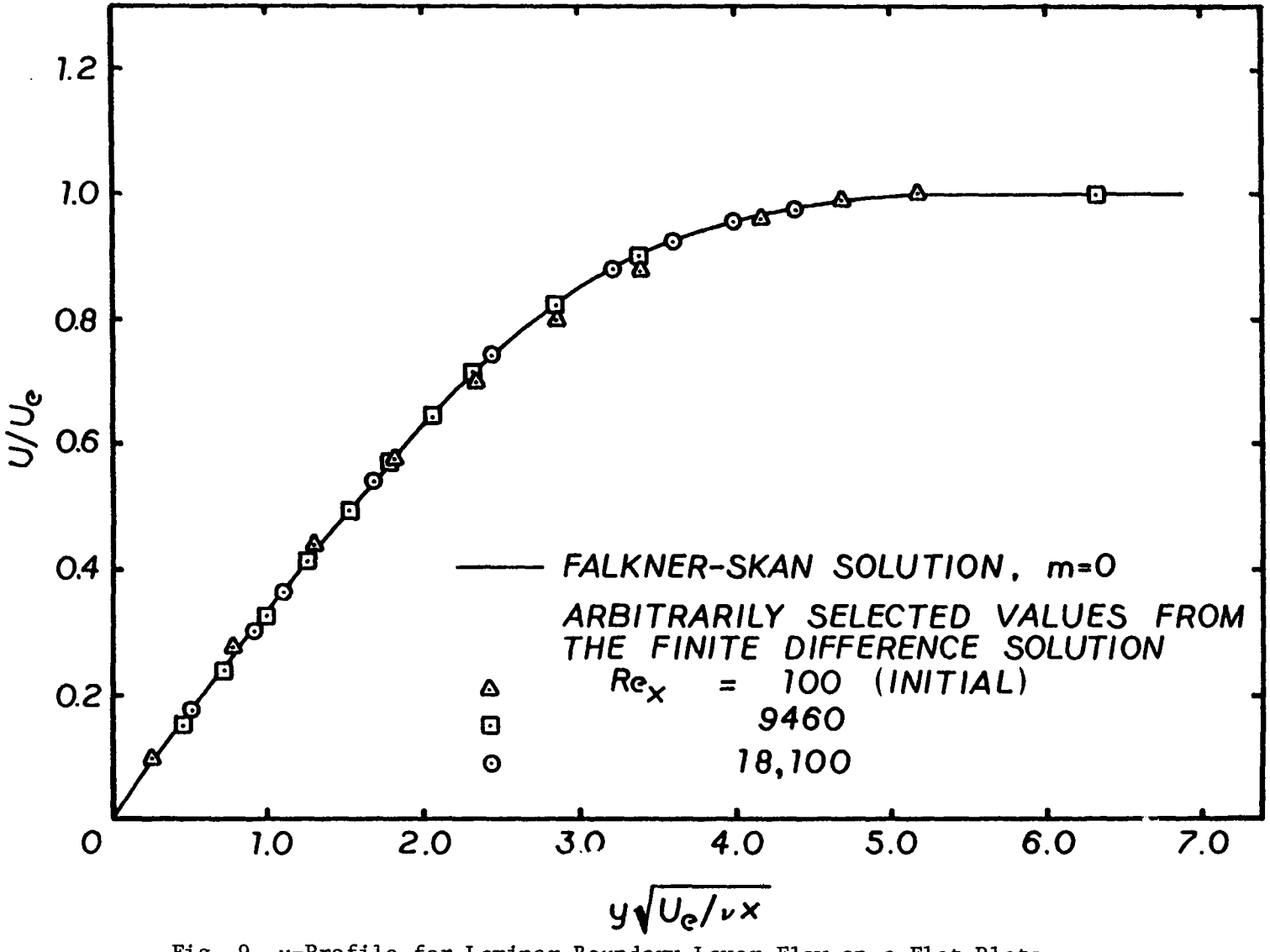

Fig. 9 u-Profile for Laminar Boundary-Layer Flow on a Flat Plate

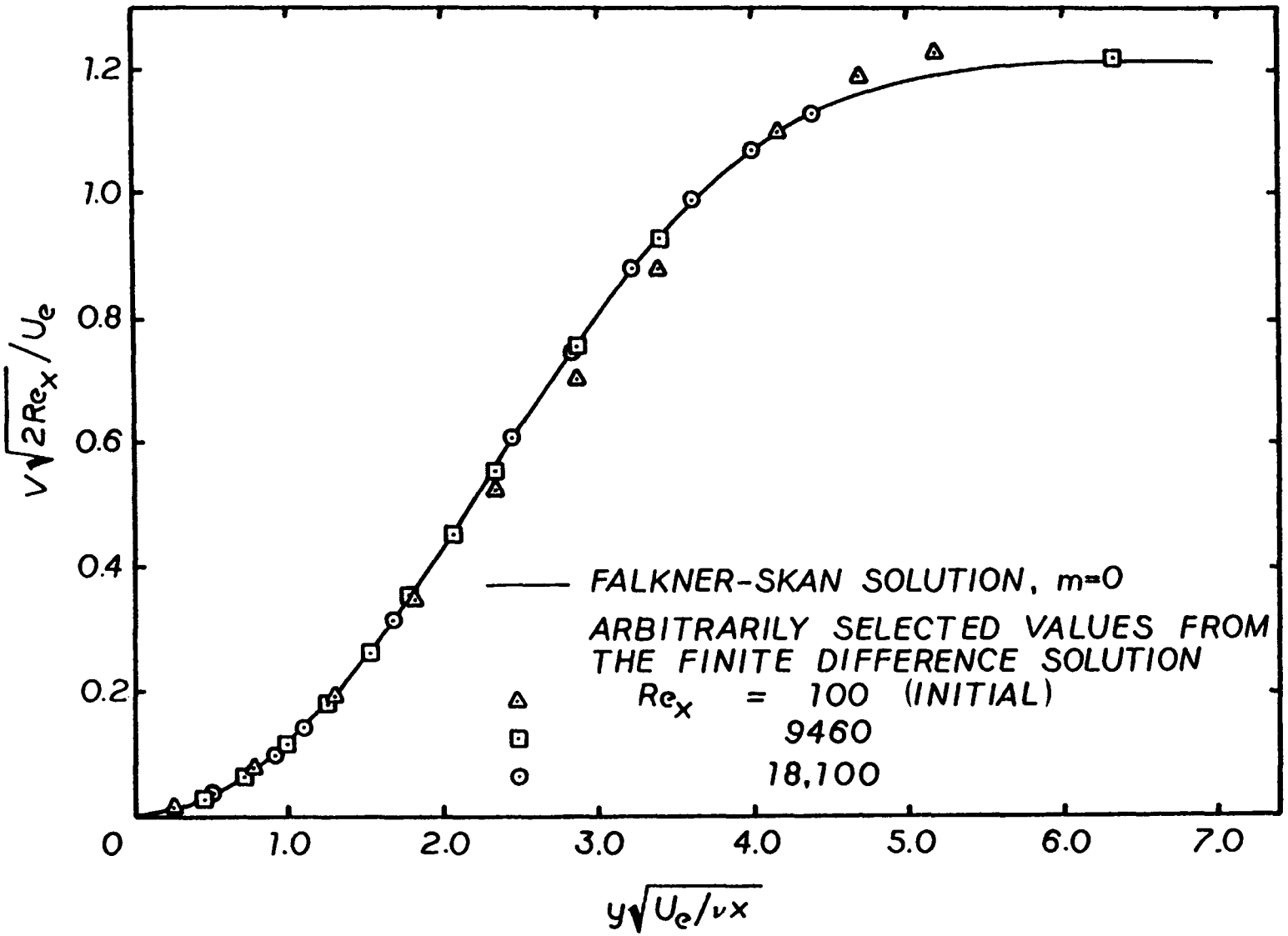

Fig. 10 v-Profile for Laminar Boundary-Layer Flow on a Flat Plate

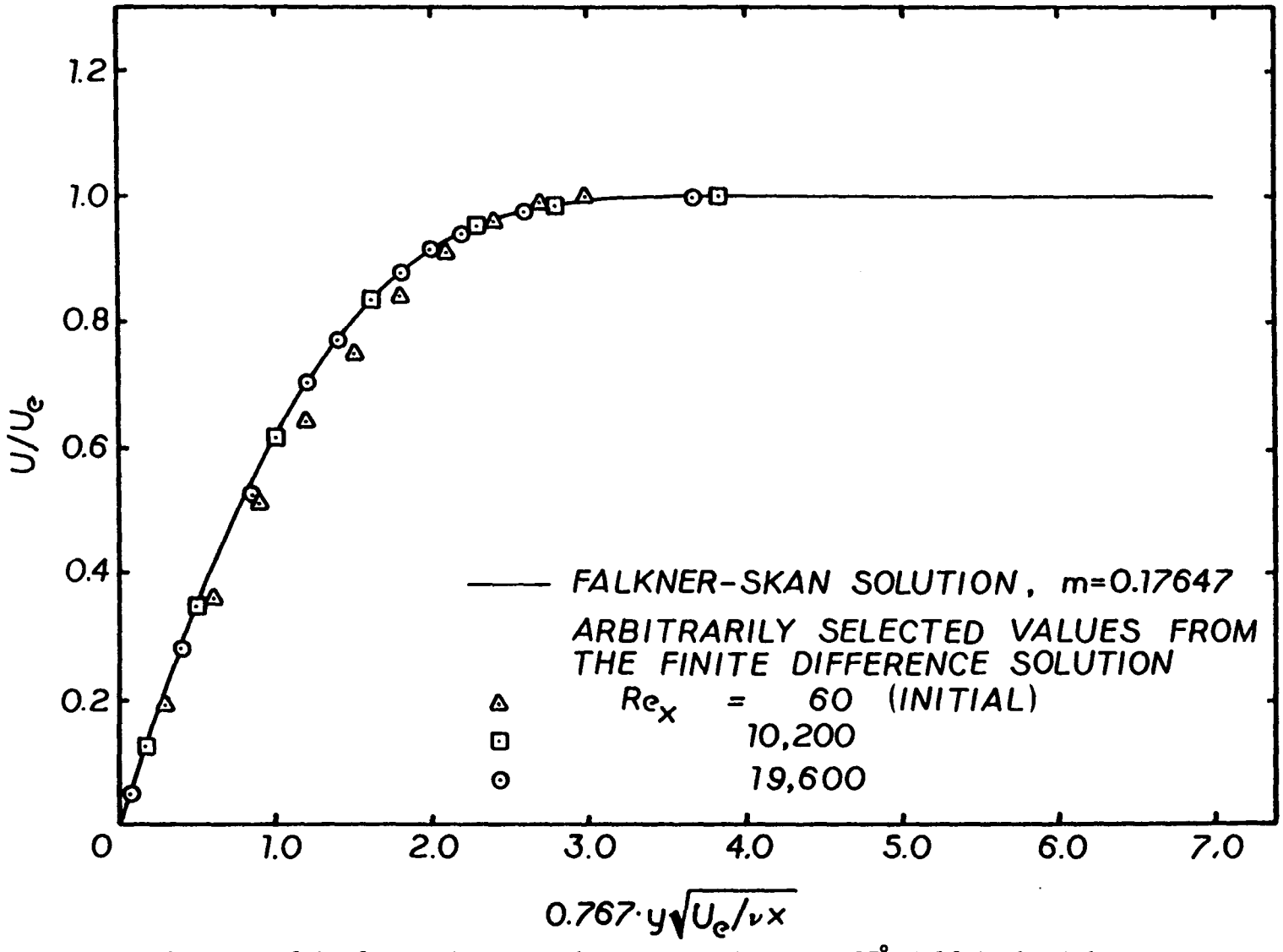

Fig. 11 u-Profile for Laminar Boundary-Layer Flow on a 27° Half-Angle Wedge

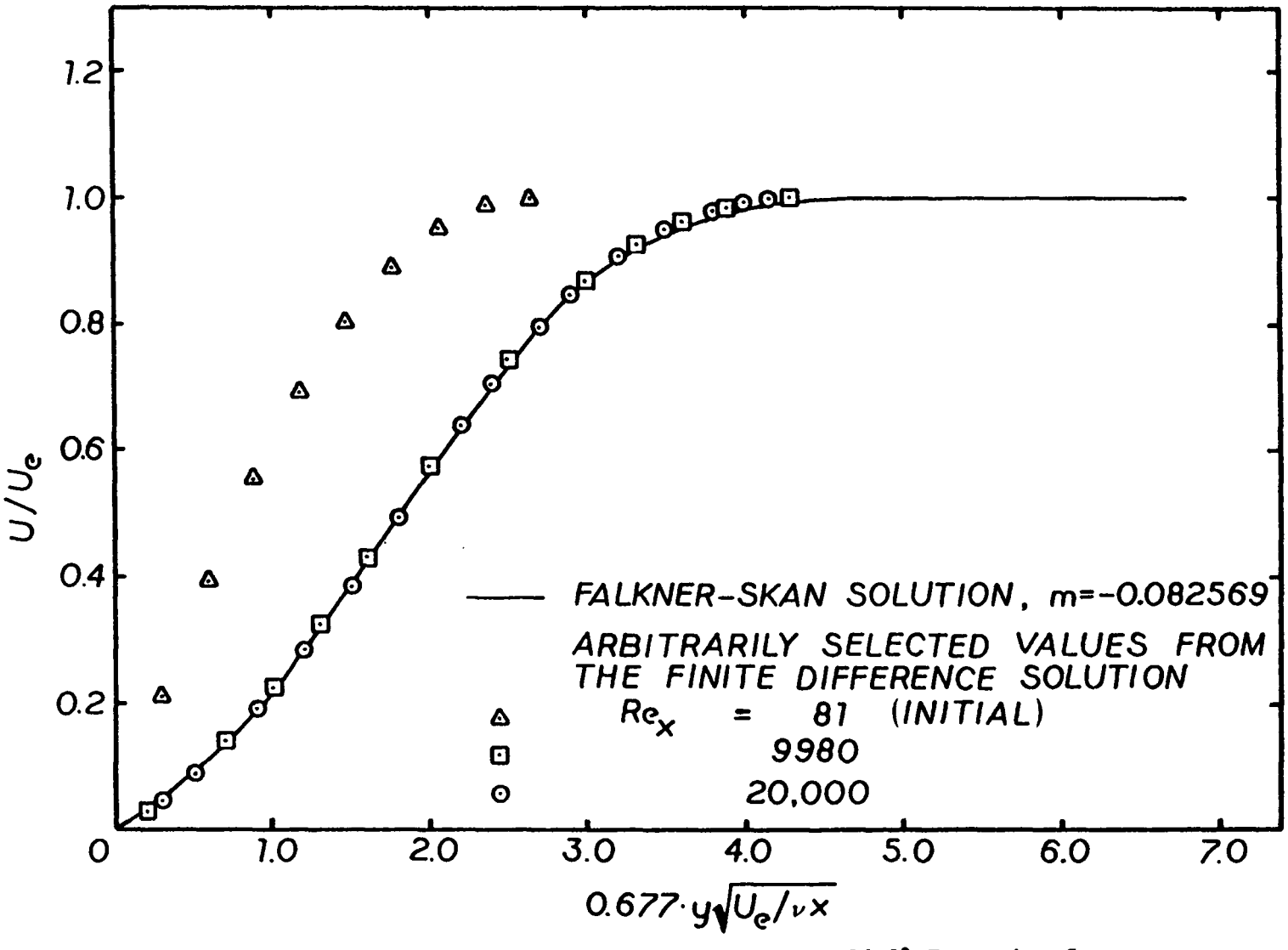

Fig. 12 u-Profile for Laminar Boundary-Layer Flow on a 16.2° Expansion Corner

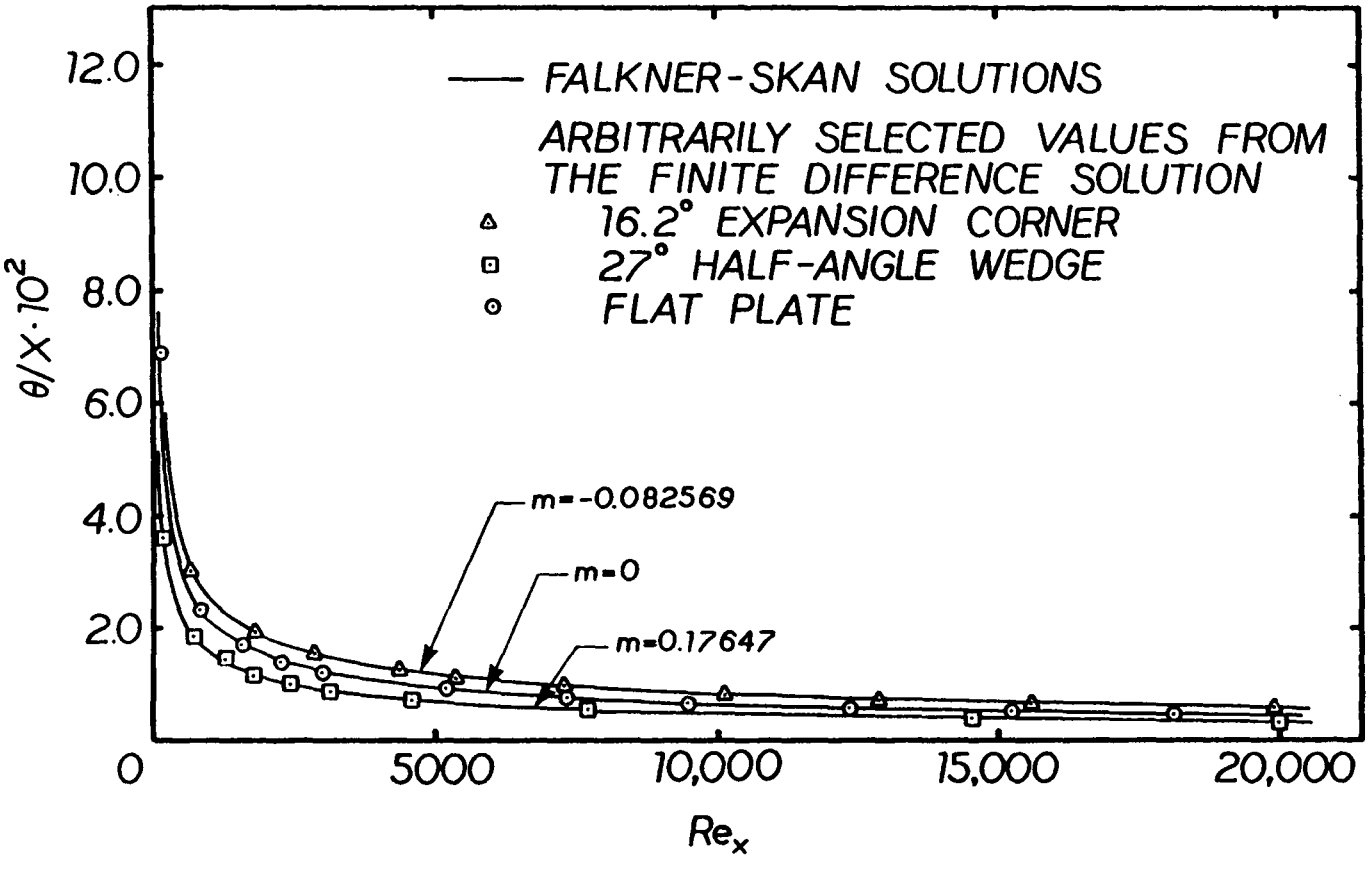

Fig. 13 Momentum Thickness for Various Laminar Boundary-Layer Flows

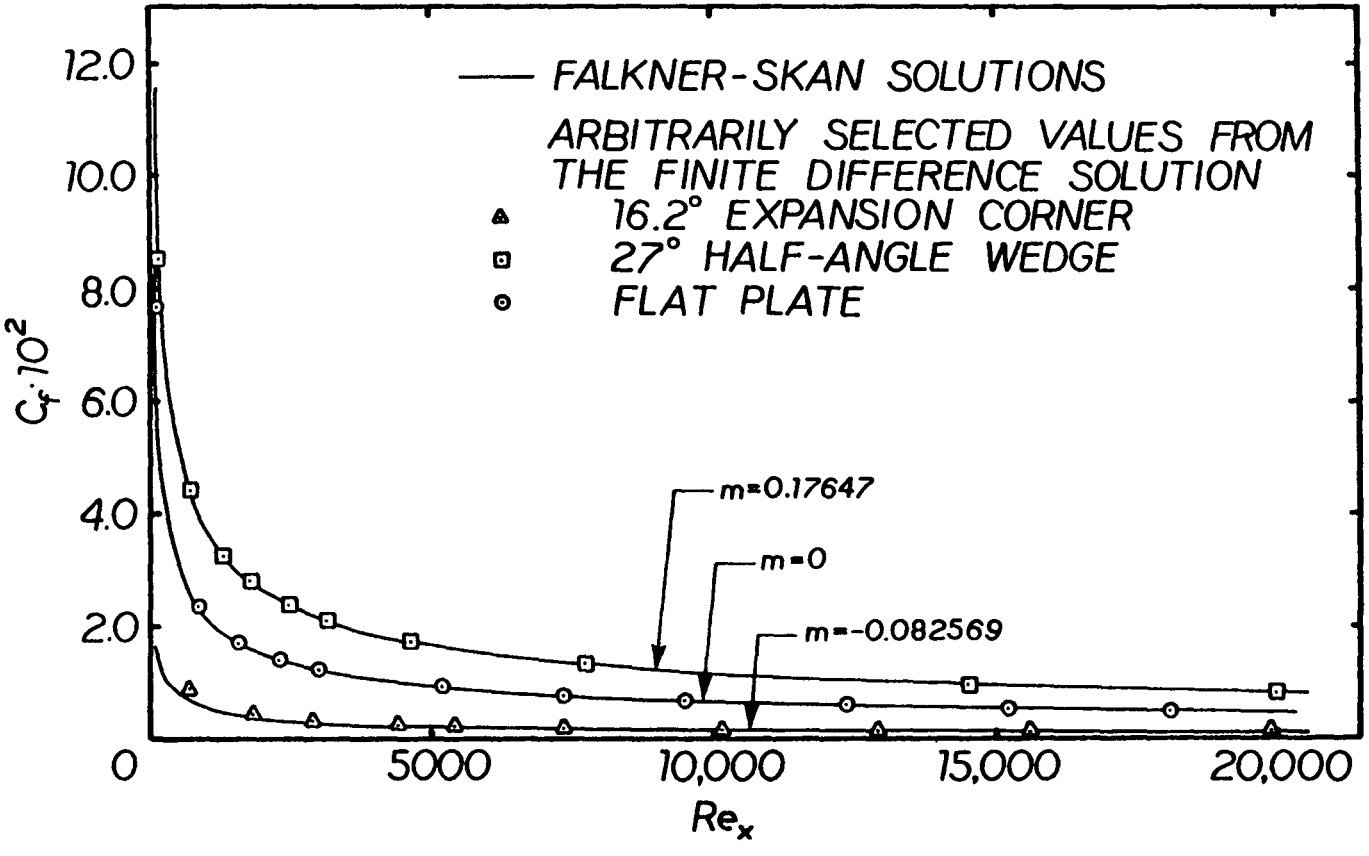

Fig. 14 Skin Friction Coefficient for Various Laminar Boundary-Layer Flows

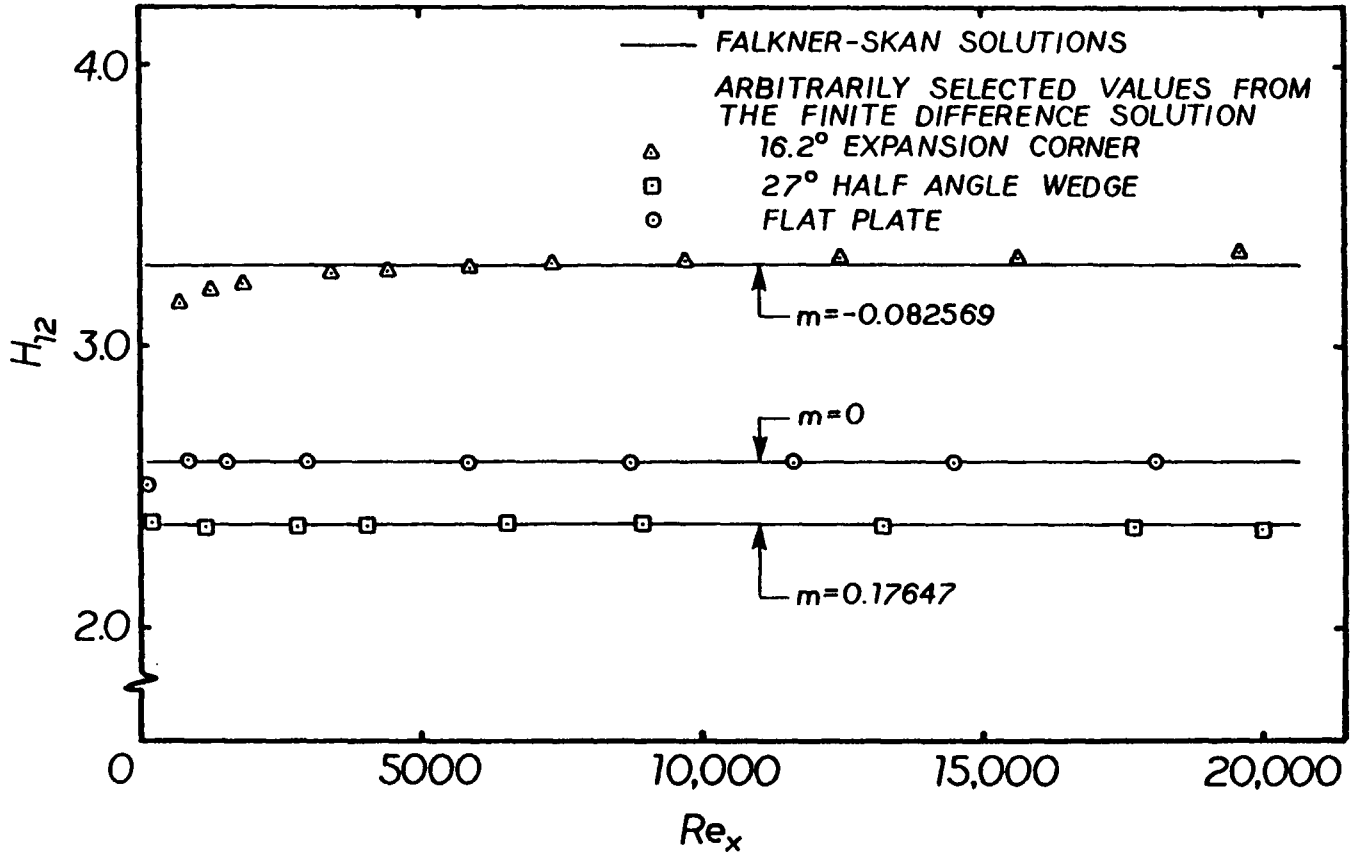

Fig. 15 Shape Factor for Various Laminar Boundary-Layer Flows

solutions. Differences as high as 10 per cent between the calculated skin friction coefficient and the value given by the similarity solution were noted for the expansion corner calculation. The discrepancy can be attributed to the step-size in the downstream direction. The Crank-Nicolson algorithm was observed to be quite sensitive to the downstream step-size for the adverse pressure gradient calculation. The laminar calculations were conducted using downstream steps on the order of the initial boundary layer thickness for the zero and favorable pressure gradient calculations and a step of approximately one-fourth of the initial boundary layer thickness for the adverse pressure gradient flow. Figure 15 gives some indication of the downstream distance required for the calculation to relax from the assumed initial boundary layer thickness and velocity distributions to the proper solution. The finite difference solution relaxes to the similarity solution rapidly for the zero and favorable pressure gradient flows. The relaxation distance is much greater for the adverse pressure gradient flow.

As shown by the range of Reynolds numbers in Fig. 9 - Fig. 12, all calculations were begun near the leading edge (for the flat plate) or the vertex (for the wedge and expansion corner) of the geometries. Pressure gradients are severe in these regions. Thus it is believed that these flows are stringent tests of the calculation procedure. The algorithm was also applied to the flow into the leading edge of a flat plate to check the ability of the calculation procedure to reduce a block, or slug profile to the similarity

solution. The algorithm performed adequately in this case.

4.2 Turbulent Boundary Layer Calculations

Turbulent boundary layer flow on a flat plate and on both surfaces of the cambered NACA 0012 airfoil section was considered. The results from the Crank-Nicolson finite difference algorithm are compared with the two-parameter integral analysis of Moses [17].

The turbulent boundary layer calculations on the cambered NACA 0012 airfoil section were performed for ideal conditions in the TRL cascade facility. The facility has incorporated a centrifugal blower powered by a 1.49 kw motor. It is assumed that the motor power capacity is delivered to the air flowing through the cascade with no increase in static pressure or temperature. Thus, the motor power is converted to the kinetic energy of the air entering the cascade tunnel. The tunnel cross section has an area of 0.0265 m^2. The cambered NACA 0012 airfoil was constructed with a blade span of 0.102 m and pitch of 0.117 m. A simple energy balance applied to the cascade air delivery equipment yields a mean velocity entering the cascade blade channel of 46.6 m/sec and a mass flow per blade channel of 0.619 kg/sec. Ambient conditions were assumed to be 27 C and $9.63 \cdot 10^4$ Pa.

The idealized cascade conditions were used in the potential flow solution of Katsanis [18] to determine the pressure gradient driving the boundary layer flow. Figure 16 shows the input data for the potential flow code. The results of the potential flow solution are

```
SUBSONIC BLADE-TO-BLADE INVISCID FLOW PROGRAM                PROGRAM TSONIC

WESKAT DATA SET FOR NACA0012 CASCADE BLADES (ALPHAI=0.0,ALPHAE=60.0,P=0.1171)

     GAM              AR              TIP            RHOIP            WTFL                                OMEGA            ORF
 0.150000E 01    0.100000E 04    0.100000E 07    0.111800E 01    0.619100E 00    0.0                 0.0              0.0
    BETAI           BETAO           CHORDF           STGRF
 0.0             -0.534800E 02    0.107960E 00   -0.162640E 00
   REDFAC          DENTOL          CUTOFF
 0.100000E 01    0.100000E-01    0.800000E 00

MBI  MBO              MM  NBBI  NBL NRSP
11   41    0    0     51   30    30    2

  BLADE SURFACE 1  --  UPPER SURFACE
     RI1             RO1             BETI1           BETO1           SPLNO1
 0.176600E-02    0.883000E-03    0.550000E 02   -0.625000E 02    0.170000E 02
    MSP1  ARRAY
 0.100000E 01    0.200600E-02    0.396600E-02    0.798000E-02    0.113690E-01    0.162020E-01    0.242590E-01    0.320200E-01
 0.461920E-01    0.585760E-01    0.692700E-01    0.786270E-01    0.869740E-01    0.943789E-01    0.100987E 00    0.104036E 00
 0.100000E 01
    THSP1  ARRAY
 0.100000E 01    0.493000E-02    0.666900E-02    0.850600E-02    0.935000E-02    0.889500E-02    0.646700E-02    0.193500E-02
-0.116150E-01   -0.292240E-01   -0.491850E-01   -0.706990E-01   -0.934460E-01   -0.116880E 00   -0.140844E 00   -0.153038E 00
 0.100000E 01

  BLADE SURFACE 2  --  LOWER SURFACE
     RI2             RO2             BETI2           BETO2           SPLNO2
 0.176600E-02    0.883000E-03   -0.435000E 02   -0.510000E 02    0.170000E 02
    MSP2  ARRAY
 0.100000E 01    0.183300E-02    0.350000E-02    0.673800E-02    0.932100E-02    0.130190E-01    0.190400E-01    0.249300E-01
 0.363540E-01    0.474310E-01    0.580670E-01    0.683309E-01    0.783240E-01    0.879800E-01    0.973660E-01    0.101996E 00
 0.100000E 01
    THSP2  ARRAY
 0.100000E 01   -0.503700E-02   -0.707400E-02   -0.100800E-01   -0.124590E-01   -0.150960E-01   -0.200820E-01   -0.254870E-01
-0.378650E-01   -0.523810E-01   -0.685630E-01   -0.861300E-01   -0.104971E 00   -0.124610E 00   -0.144866E 00   -0.155218E 00
 0.100000E 01

    MR  ARRAY
-0.100000E 01    0.100000E 01
   RMSP  ARRAY
 0.559100E 00    0.559100E 00
   BESP  ARRAY
 0.101600E 00    0.101600E 00

  BLDAT  AANDK  ERSOR  STRFN  SLCRD  INTVL  SURVL  ICONT  NLAST  JFLOW  JOUT  JGRAPH
    1      0      0      0      0      0      1      1      1      1      1      1
```

Fig. 16 Input to the Potential Flow Solution in the Cascade Blade Channel

shown as a dimensionless blade-surface velocity distribution in Fig. 17a. The blade-surface velocity distribution as a function of the distance along the surface of the blade is required for the boundary layer solution. Cubic spline interpolation was used to fit the blade coordinates and determine the surface length as a function of axial distance. Once the relation between surface and axial length was obtained, the surface velocity distribution was cross-plotted to obtain the velocity distribution as a function of surface distance as shown in Fig. 17b.

The results predicted by the Crank-Nicolson finite difference algorithm for turbulent boundary layer flow on a flat plate are shown in Fig. 18 - Fig. 21. Good agreement between the finite difference algorithm and Moses's integral solution is shown.

The momentum thickness and skin friction coefficient for the airfoil section are shown in Fig. 22 and Fig. 23. The two solutions exhibit the same general behavior with differences as high as 12 per cent for the skin friction coefficient and 11 per cent for the momentum thickness occurring on the suction side of the blade. The difference in the turbulent flow results lies in the assumed form of the turbulent viscosity distribution. Moses assumes the eddy viscosity distribution to be constant across the boundary layer. He draws his eddy viscosity model from zero pressure gradient experimental results. Cebeci's eddy viscosity distribution was used in the finite difference algorithm where the transverse variation as well as pressure gradient effects are incorporated into the turbulent

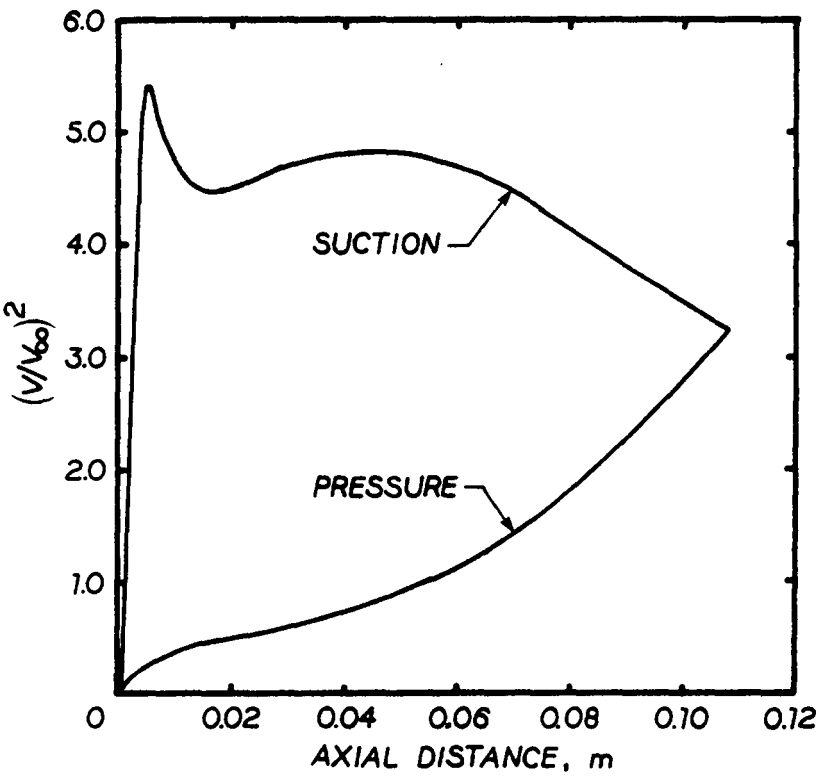

Fig. 17a Blade Surface Velocities

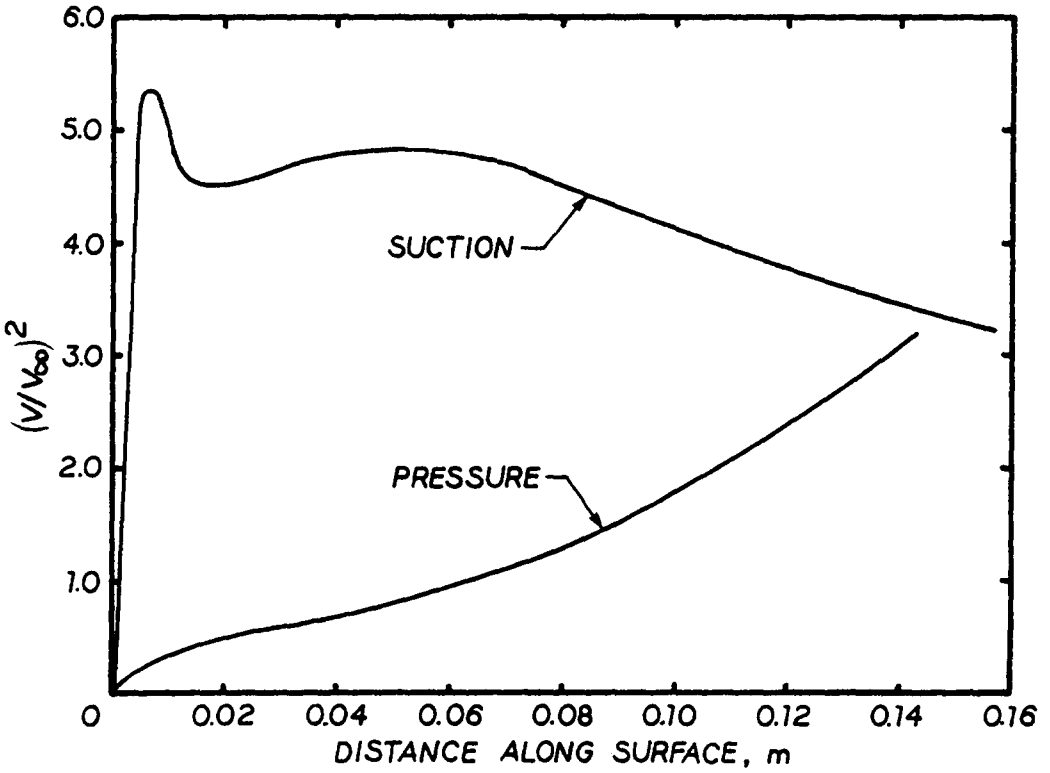

Fig. 17b Blade Surface Velocities

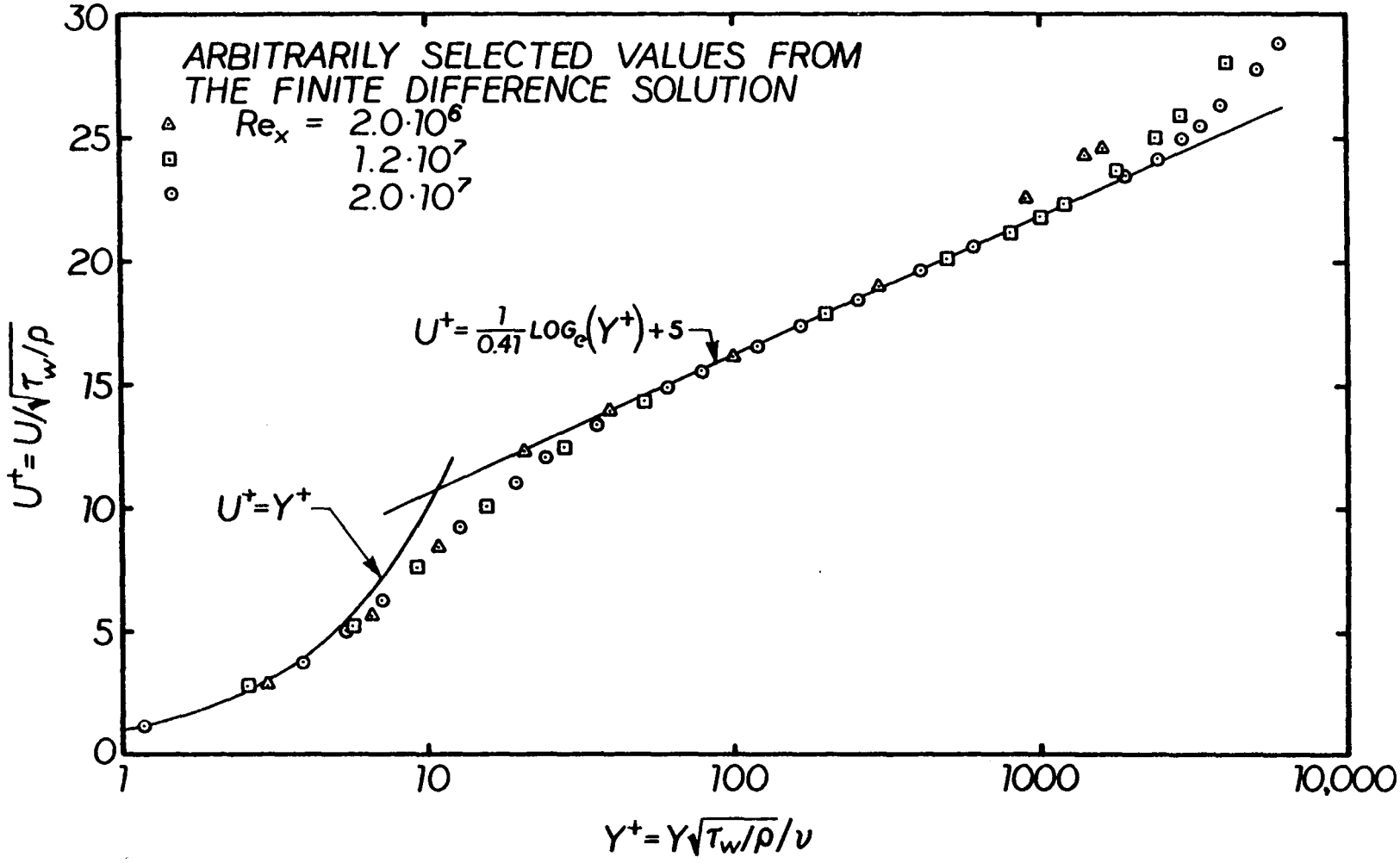

Fig. 18 u-Profile for Turbulent Boundary-Layer Flow on a Flat Plate

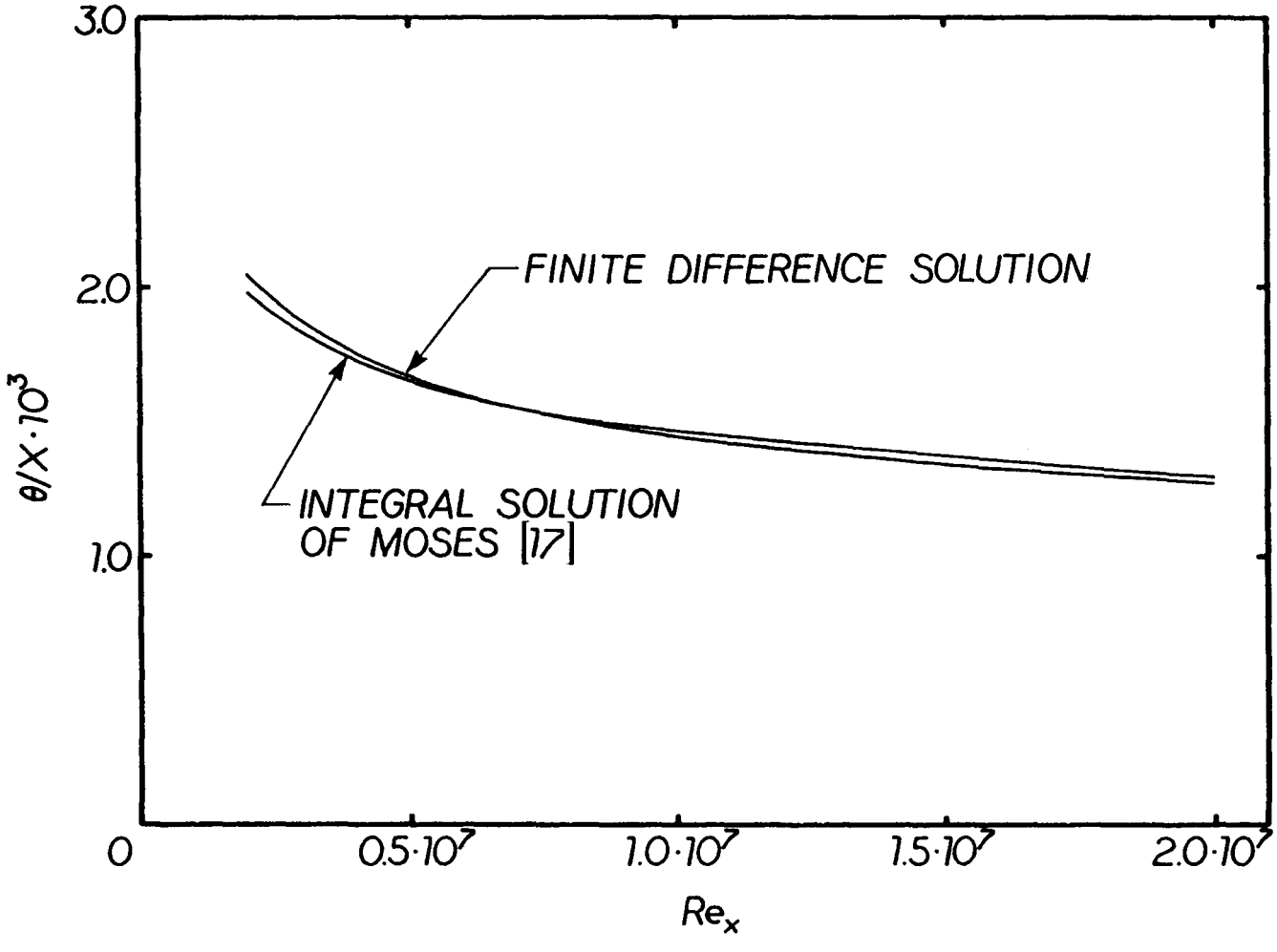

Fig. 19 Momentum Thickness for Turbulent Boundary-Layer Flow on a Flat Plate

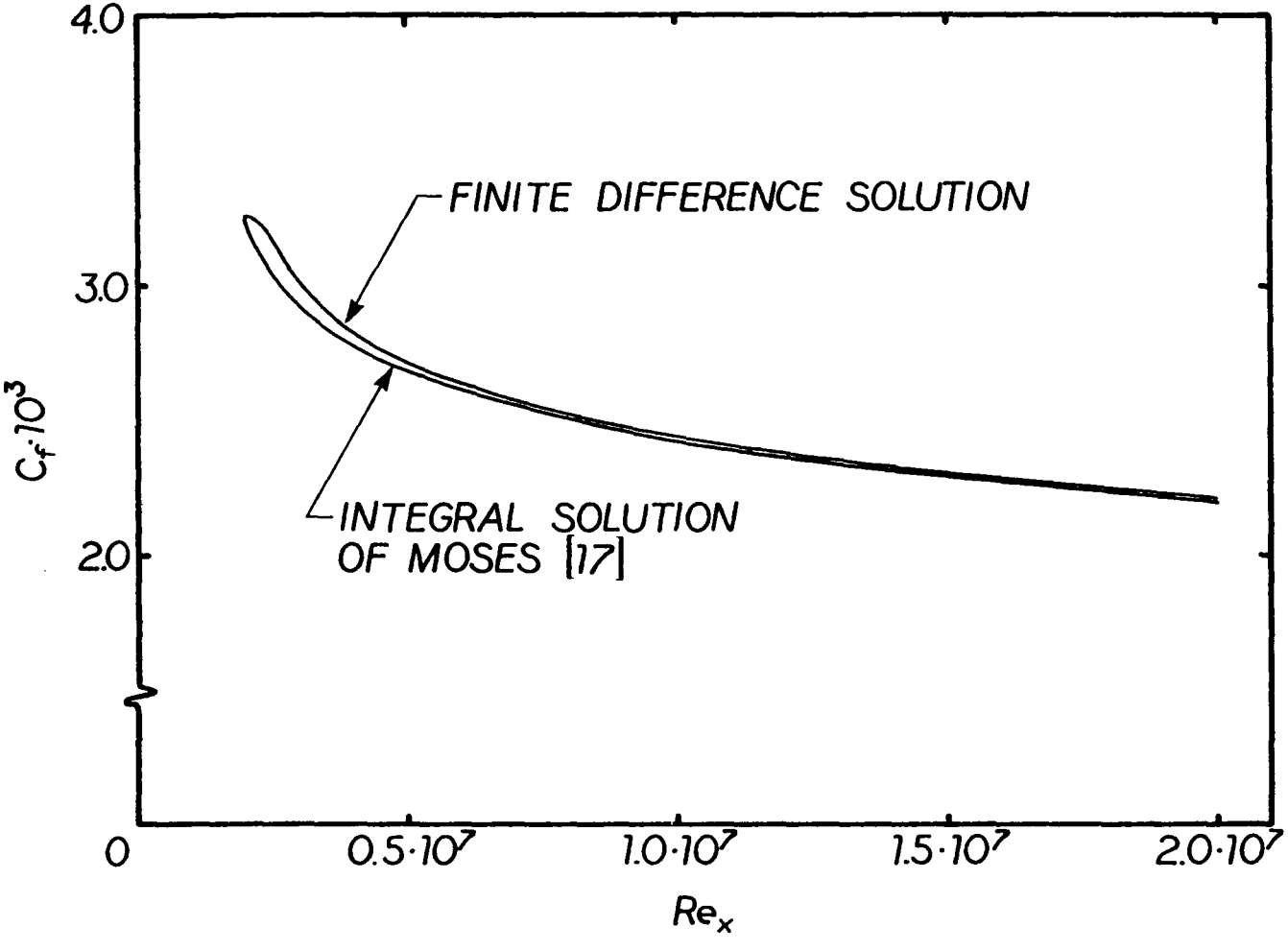

Fig. 20 Skin Friction Coefficient for Turbulent Boundary-Layer Flow on a Flat Plate

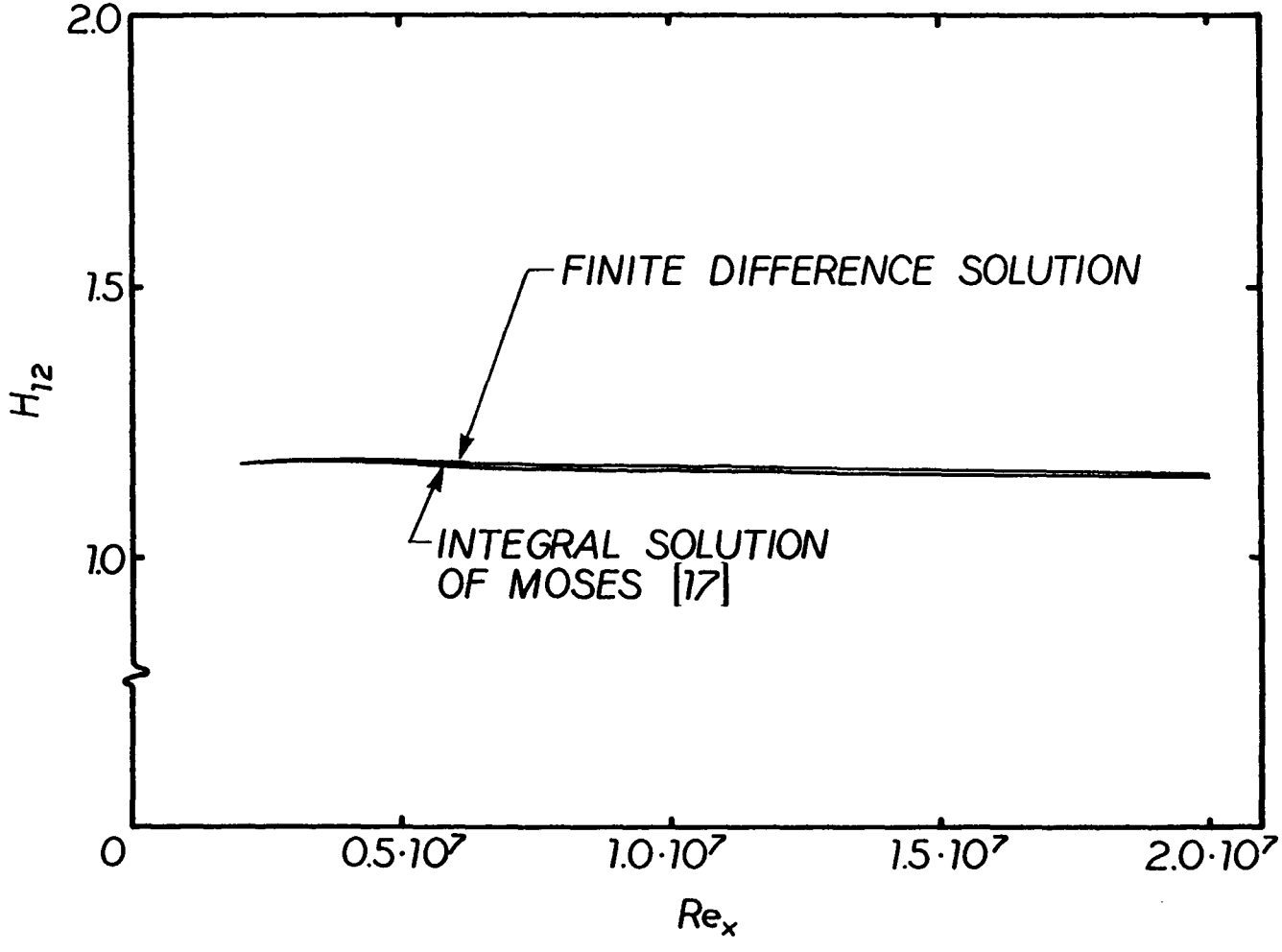

Fig. 21 Shape Factor for Turbulent Boundary-Layer Flow on a Flat Plate

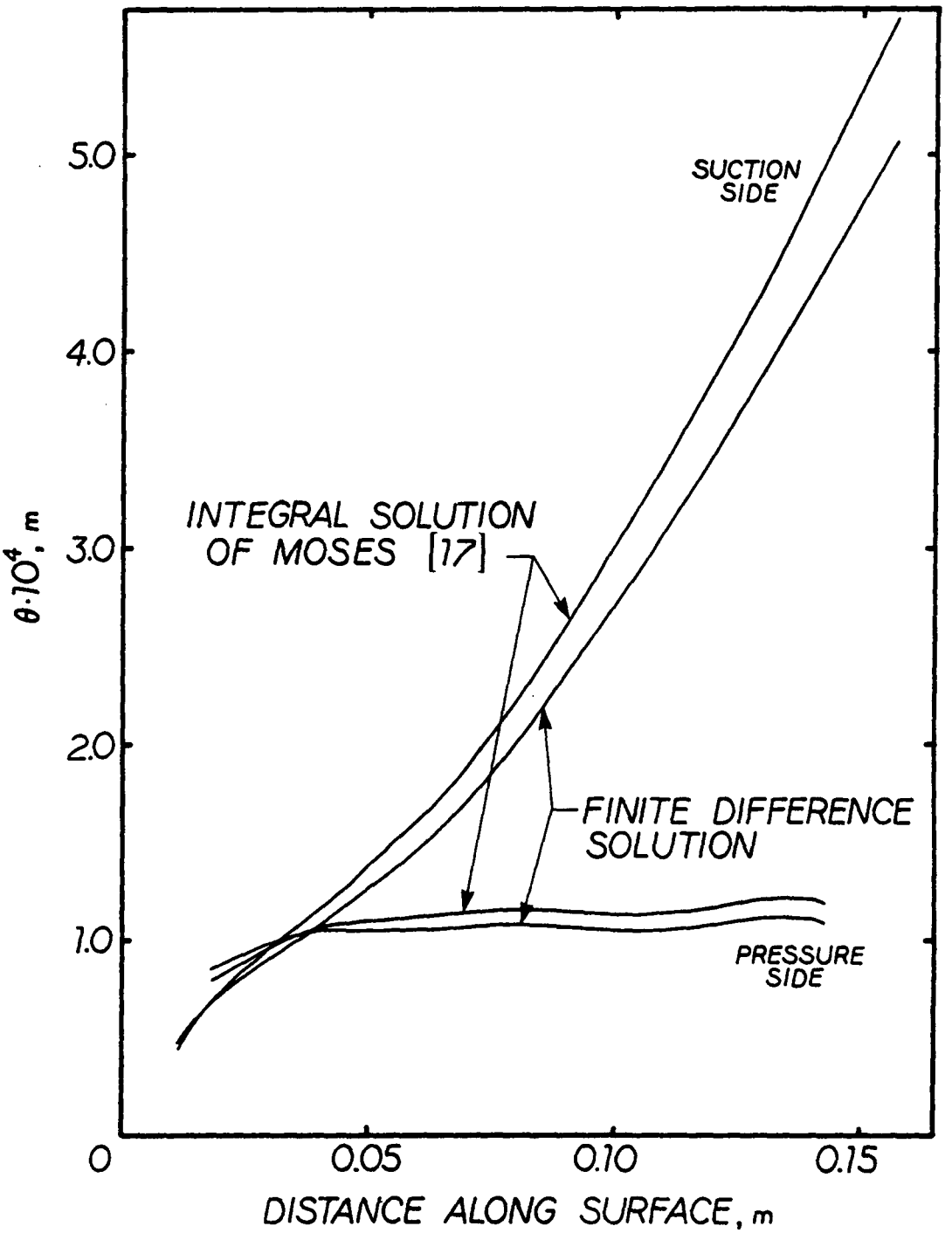

Fig. 22 Momentum Thickness on Cambered NACA 0012 Airfoil Section

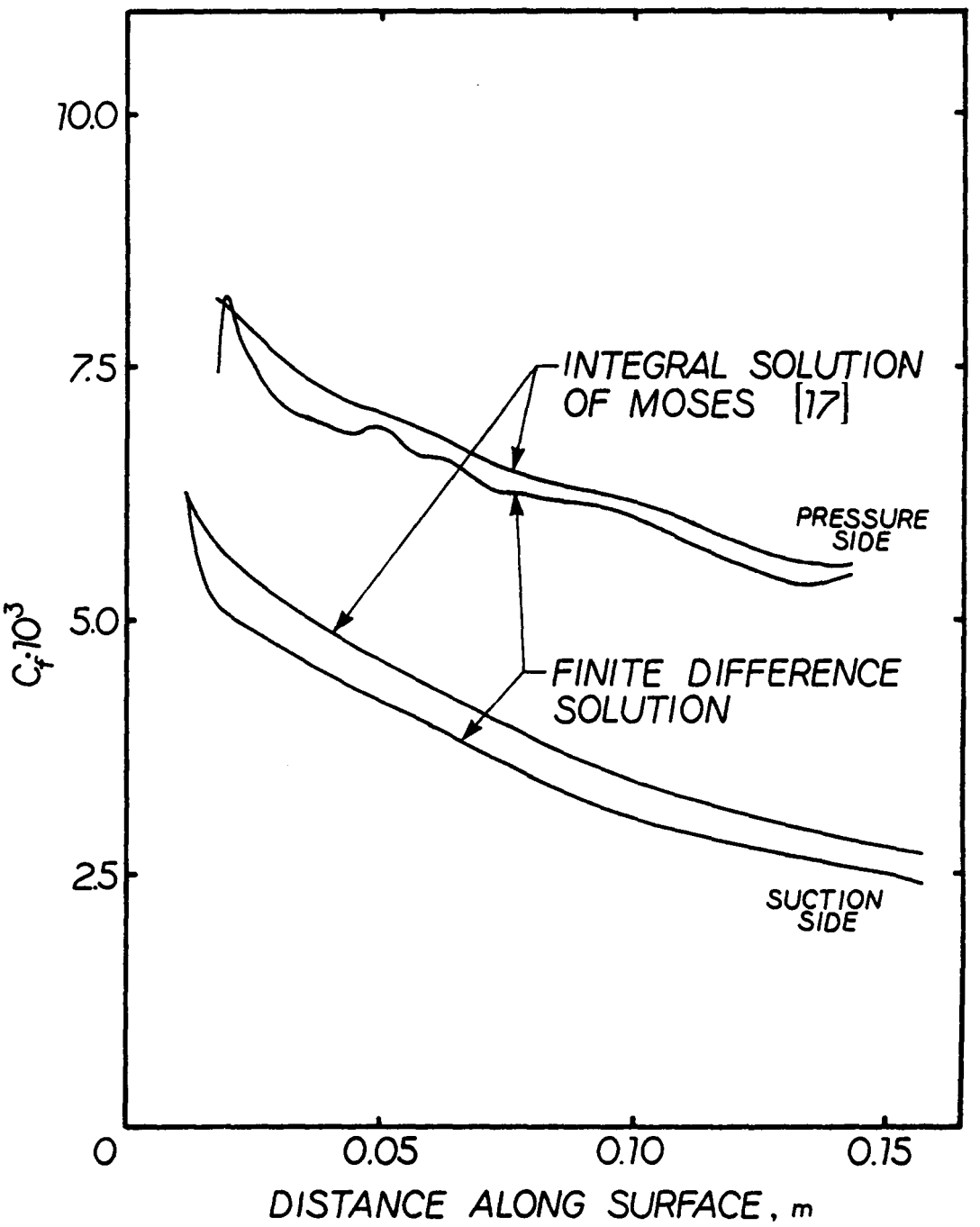

Fig. 23 Skin Friction Coefficient on Cambered NACA 0012 Airfoil Section

viscosity model. The good agreement for zero pressure gradient flow between the two calculations follows from the nature of Moses's eddy viscosity model.

The turbulent boundary layer calculations on the blade surfaces were started at locations corresponding to 10 per cent of the camber line length. The flat-plate approximation for the initial boundary layer development yielded thicknesses of $4.50 \cdot 10^{-4}$ m and $8.10 \cdot 10^{-4}$ m for the suction and pressure sides respectively.

4.3 Wall-Jet Calculations

The interaction of the wall jet with the initial boundary layer development in zero pressure gradient laminar and turbulent boundary layer flow was investigated. The calculations were performed for the ratios $\delta_i/s=0.5$ and $V_j/u_e=1.0$. Figure 24 and Fig. 25 show the predicted development of the boundary layer u-profile downstream from the injection point. The decay of the injected profiles may be characterized by the prominence of the relative minimums and maximums in the velocity profiles. The laminar profiles exhibit prominent points of relative minimums and maximums through 51 slot heights downstream from the point of injection. For turbulent flow, the characteristic shape is barely visible after 40 slot heights downstream from the injection point. The rapid mixing effect was expected for the turbulent jet due to the gross eddying action characteristic of turbulent flow.

The wall-jet calculation on the cambered NACA 0012 airfoil

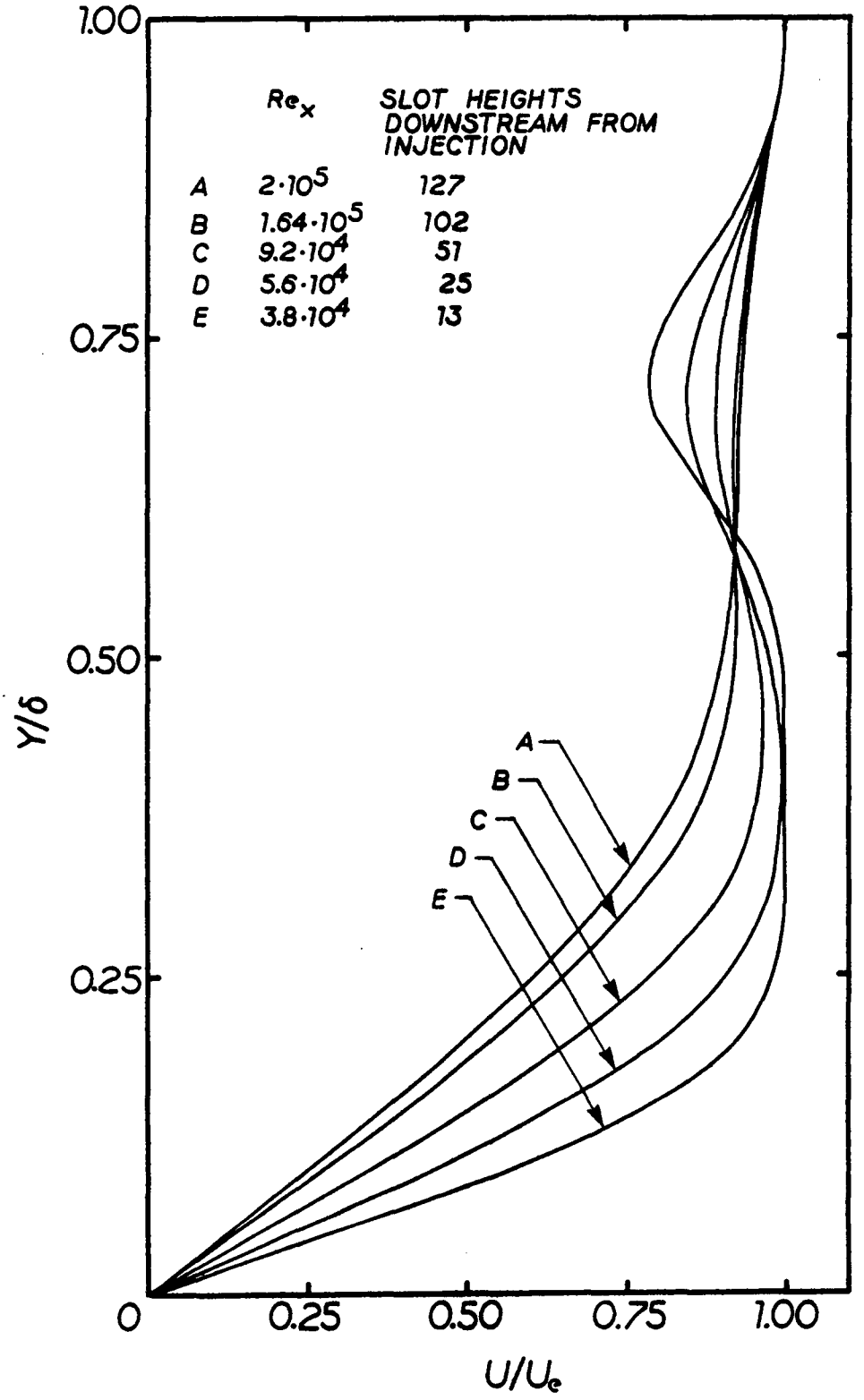

Fig. 24 u-Profile on a Flat Plate with Tangential Injection -- Laminar, $\delta_i/s = 0.5$, $V_j/u_e = 1.0$

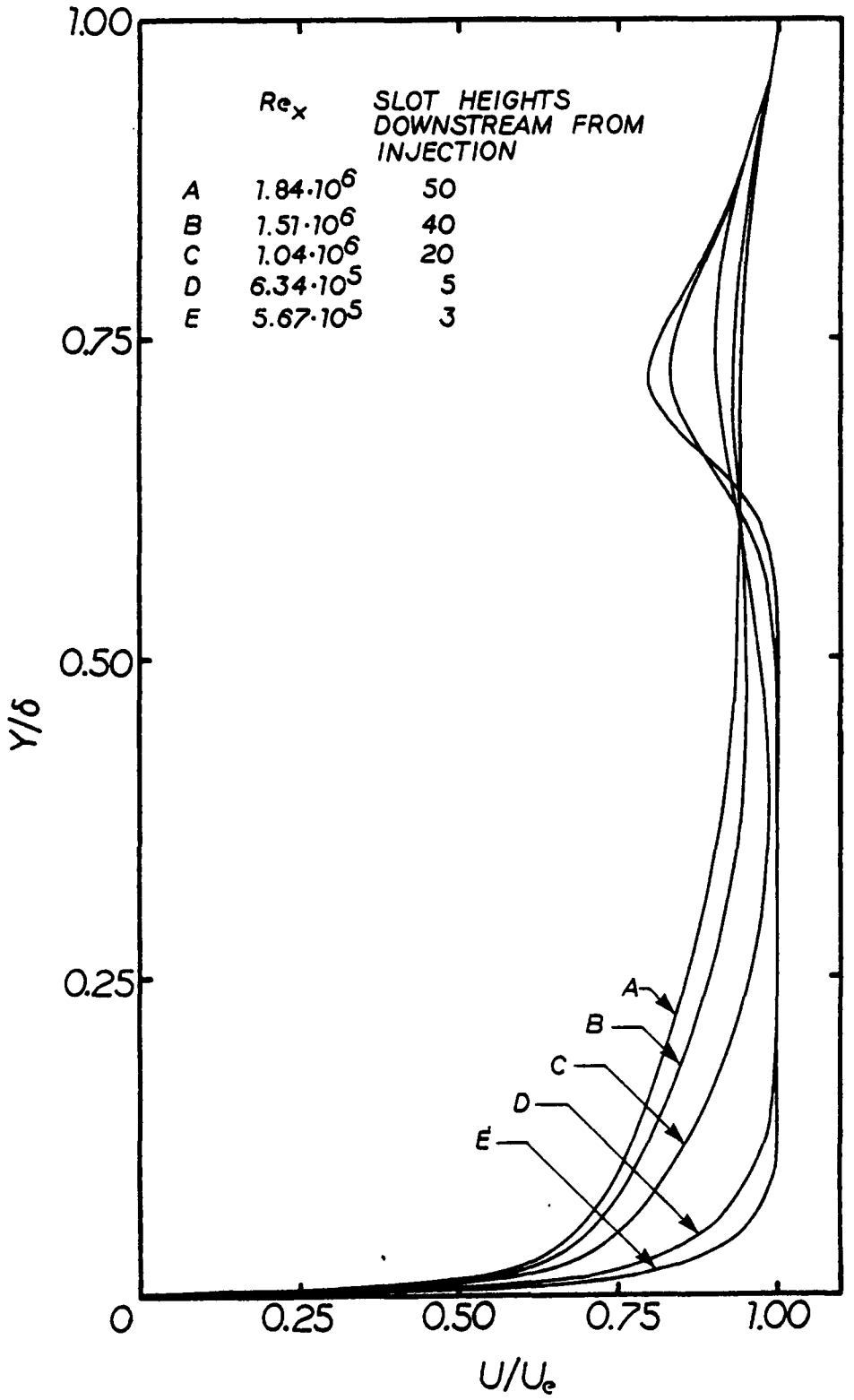

Fig. 25 u-Profile on a Flat Plate with Tangential Injection -- Turbulent, $\delta_i/s = 0.5$, $V_j/u_e = 1.0$

section was begun at 10 per cent of the camber line length. Again, the wall jet was constructed with the ratios $\delta_i/s=0.5$ and $V_j/u_e=1.0$. Figure 26 and Fig. 27 show the momentum thickness and skin friction coefficient for the injected boundary layer on the blade section. A large increase in the skin friction for the injected boundary layer with respect to the conventional case occurs. The skin friction coefficient for the injected boundary layer is most certainly affected by the wall-jet model where a high velocity gradient near the wall results from the slug flow approximation. A more realistic model for the flow issuing from the wall jet would be the velocity profile resulting from an analysis of the turbulent flow between infinite parallel plates. The momentum thickness on the suction side of the blade is shown to be approximately $3.5 \cdot 10^{-5}$m greater than the non-injected boundary layer. On the pressure side of the blade, the momentum thickness shows a rapid increase over the non-injected boundary layer within 14 slot heights downstream from the point of injection--declining from this point owing to the favorable pressure gradient along the pressure side of the blade. The momentum thickness at the trailing edge of the blade for the injected boundary layer is 10 per cent and 11 per cent greater than the non-injected boundary layer for the suction and pressure sides respectively.

The u profiles on the blade section at several locations downstream from the point of injection are shown in Fig. 28 and Fig. 29. The characteristic shape of the injected profiles persists through 30 slot heights downstream from the injection point on the suction

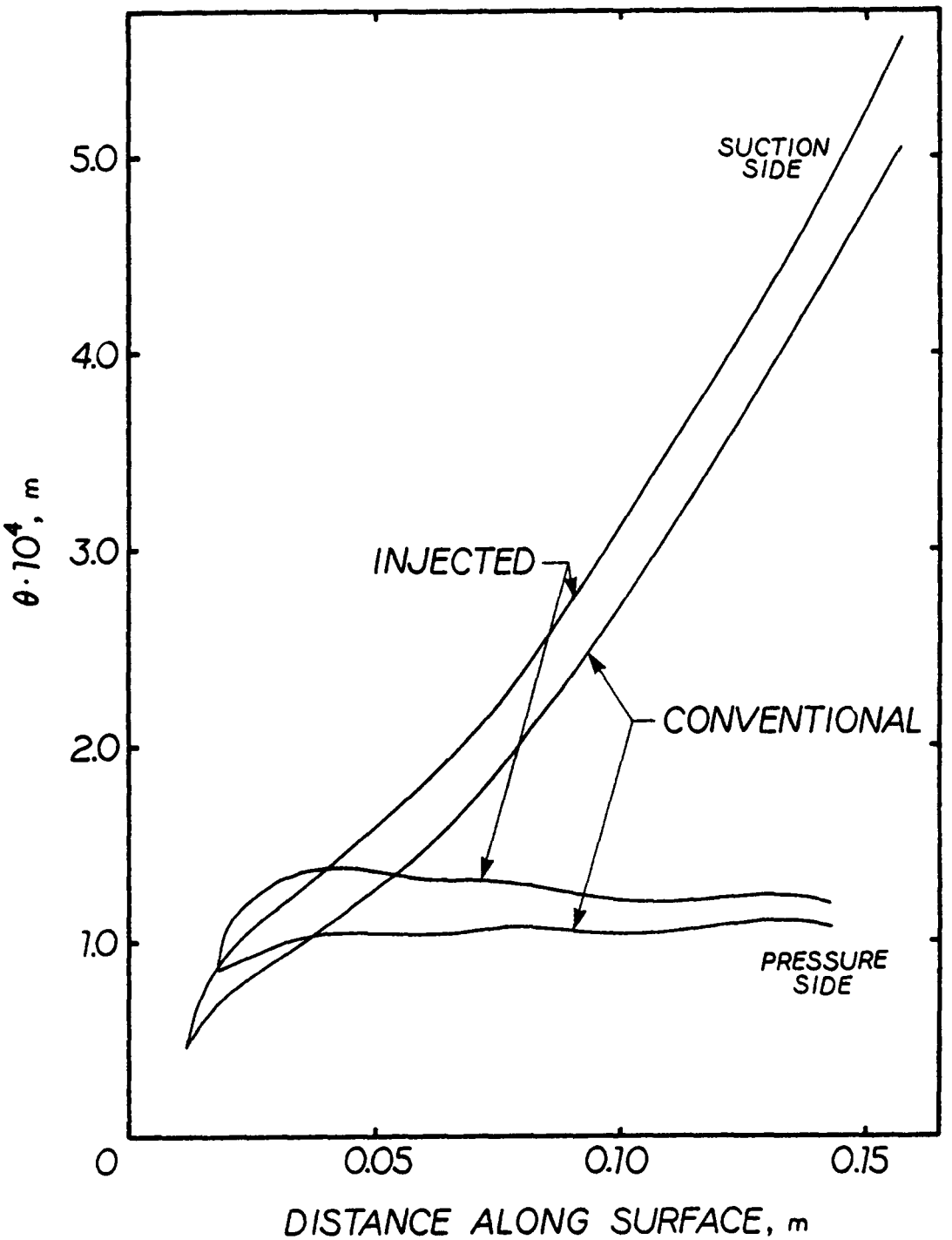

Fig. 26 Momentum Thickness on Cambered NACA 0012 Airfoil Section with Tangential Injection Near the Leading Edge -- $\delta_i/s = 0.5$, $V_j/u_e = 1.0$

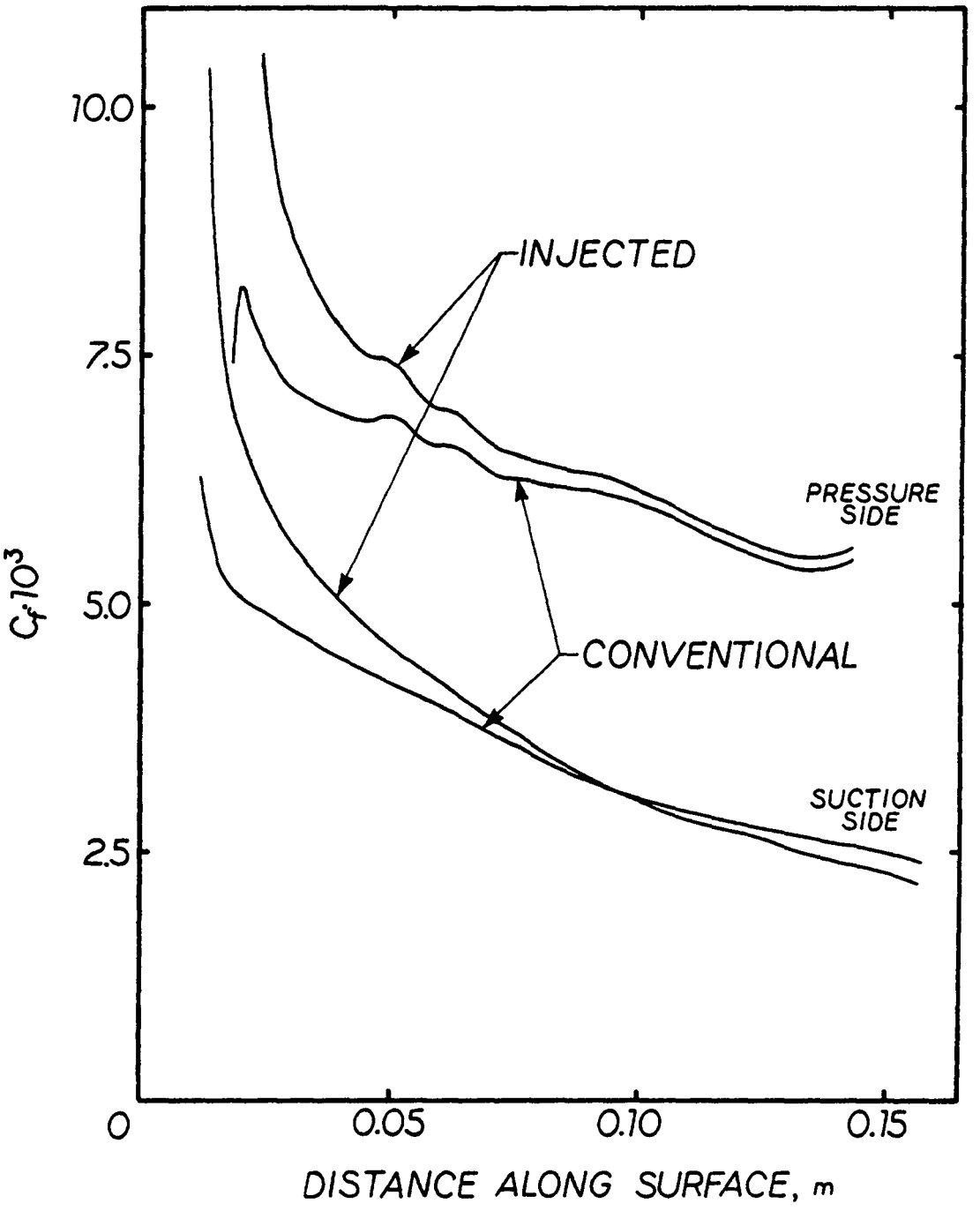

Fig. 27 Skin Friction Coefficient on Cambered NACA 0012 Airfoil Section with Tangential Injection Near the Leading Edge -- $\delta_i/s = 0.5$, $V_j/u_e = 1.0$

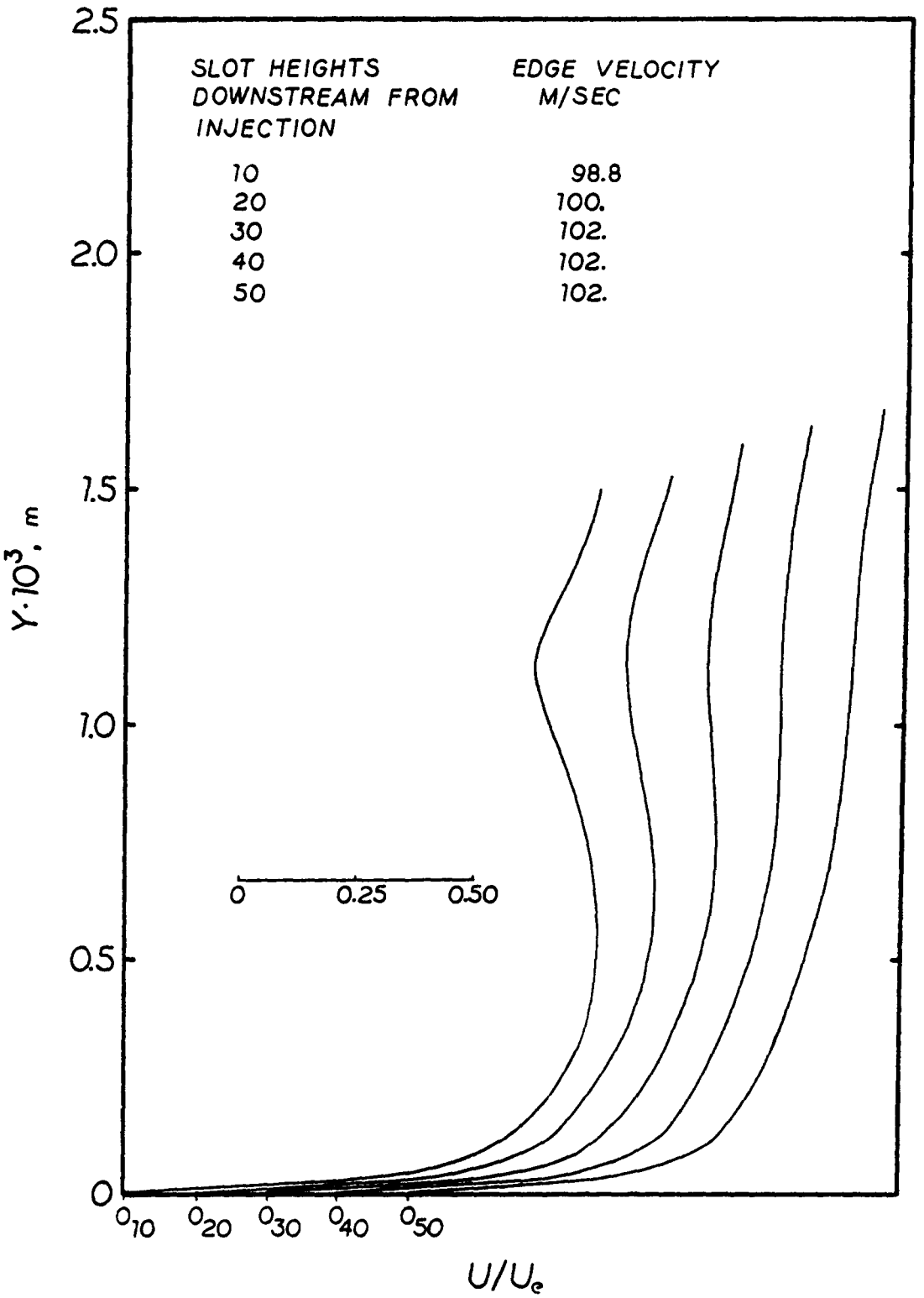

Fig. 28 u-Profiles on Suction Side of Cambered NACA 0012 Airfoil Section Downstream from Tangential Injection -- $\delta_i/s = 0.5$, $V_j/u_e = 1.0$

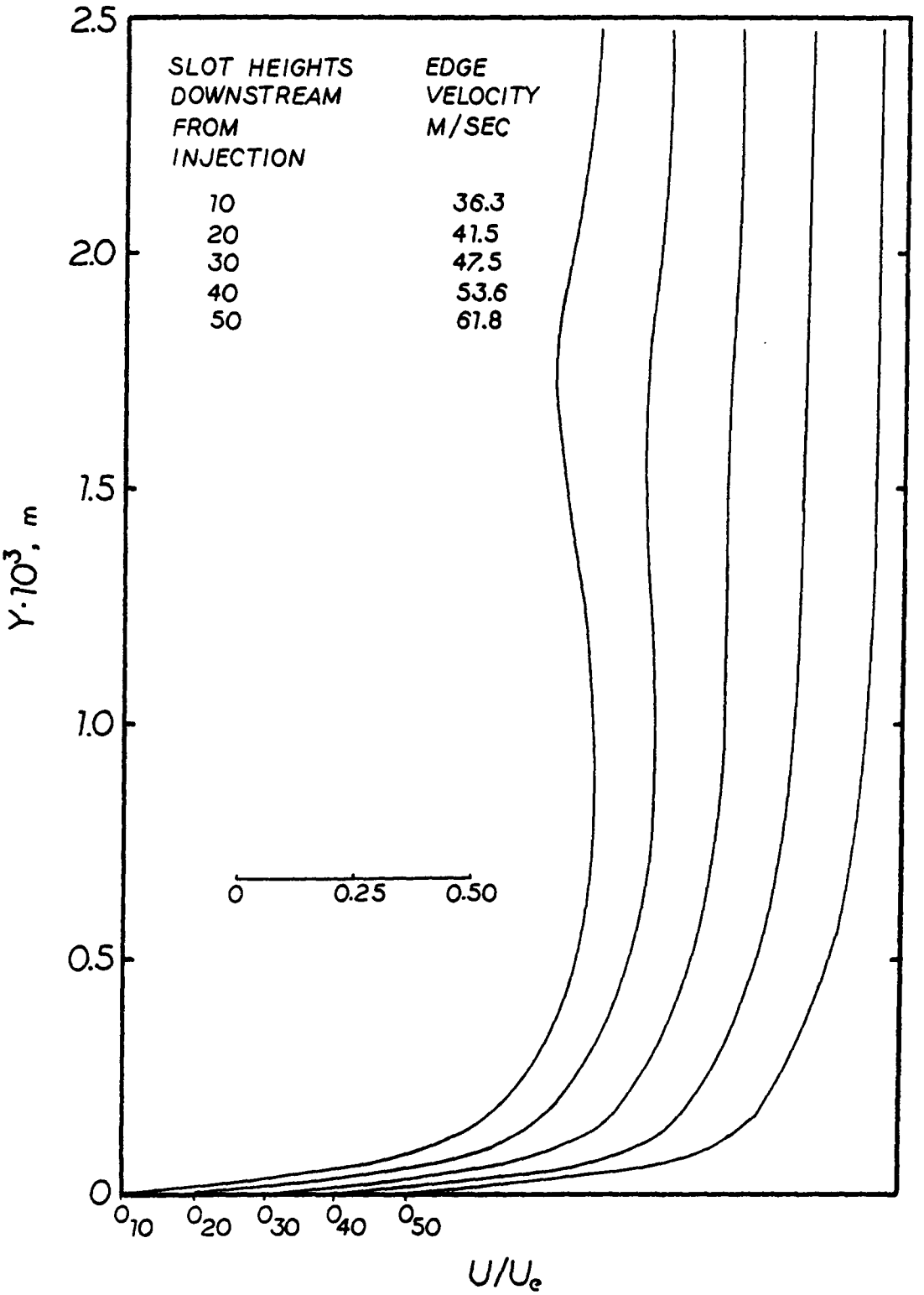

Fig. 29 u-Profiles on Pressure Side of Cambered NACA 0012 Airfoil Section Downstream from Tangential Injection -- $\delta_i/s = 0.5$, $V_j/u_e = 1.0$

side of the blade versus 20 slot heights for the pressure side.

The downstream step-size required for the prediction of the injected boundary layer development was smaller than the downstream step utilized in the conventional boundary layer calculations. Downstream steps of 20 per cent and 1.7 per cent of the total boundary layer thickness (including the slot height) at the initial station were used in the wall-jet calculations with no pressure gradient. Downstream steps of 0.24 per cent and 1 per cent of the total boundary layer thickness at the point of injection were necessary to predict the boundary layer flow on the pressure and suction sides of the blade. In all cases investigated, the step-size was determined by solving the governing equations using a step-size equal to the initial boundary layer thickness. The downstream step was repeatedly halved until two solutions, one with a step of Δx and a second with a step of $\Delta x/2$, produced the same results.

5. Conclusions and Recommendations for Further Study

The Crank-Nicolson finite difference algorithm employed in the solution to the boundary layer equations was found to perform well when applied to conventional boundary layer flows. The predicted results from the finite difference algorithm were found to agree well with the Falkner-Skan similarity solutions for three laminar boundary layer flows: flow into a 27° half-angle wedge, flow on a flat plate, and flow around a 16.2° expansion corner. The finite difference predictions were also found to agree well with an integral solution for turbulent boundary layer flow on a flat plate and on representative combustion turbine blade surfaces. The algorithm was found to be capable of predicting the behavior of the boundary layer downstream from the tangential injection of a second stream.

Further efforts to utilize the algorithm should be conducted in the following areas.

(i) An eddy viscosity model applicable to the mixing of some initial boundary layer development with the flow issuing from a tangentially oriented wall jet should be sought. It is recognized that the two-layer model used in the solutions presented may not prove to be an accurate description of the ε variation in wall-jet flow. The high gradients at the wall near the injection point resulting from the slug flow approximation were found to switch the ε model to

the outer law prematurely.

(ii) A more efficient means of controlling the downstream step-size other than simply using a constant downstream step is possible. The selection of the downstream step-size was found to be sensitive to pressure gradient and the nature of the initial velocity profile (conventional or injected profile). One technique which could be employed is

$$\Delta x = \text{constant} \cdot \delta_i \left(1 - \frac{1}{u_e} \cdot \frac{du_e}{dx}\right)$$

where the constant is selected according to the nature of the initial profile.

(iii) The equation governing conservation of energy along with a suitable equation of state should be incorporated into the analysis. A study of the flow of compressible gases through turbine blade passages could then be performed.

(iv) Testing of the cambered NACA 0012 blade section in the TRL cascade facility to determine the pressure gradient along the blade surfaces and the behavior of the wall jet downstream from injection near the leading edge should be initiated.

References

1. "ASME Winter Annual Meeting Report," Mechanical Engineering, Vol. 100, No. 2, Feb., 1978, pp. 78-79.

2. Goldstein, R. J., "Film Cooling," Advances in Heat Transfer, Vol. 7, Academic Press, 1971, p. 321.

3. Beckwith, I. E., and Bushnell, D. M., "Calculation by a Finite-Difference Method of Supersonic Turbulent Boundary Layers with Tangential Slot Injection," NASA TN D-6221, Langley Research Center, April, 1971.

4. Glauert, M. B., "The Wall Jet," Journal of Fluid Mechanics, Vol. 2, 1956, p. 625.

5. McGahan, W. A., "The Incompressible, Turbulent Wall Jet in an Adverse Pressure Gradient," MIT Gas Turbine Laboratory Report No. 82, September, 1965.

6. Miner, E. W., and Lewis, C. H., "A Finite-Difference Method for Predicting Supersonic Turbulent Boundary Layer Flows with Tangential Slot Injection," NASA CR-2/24, Prepared by Virginia Polytechnic Institute and State University, October, 1972.

7. Levine, J. N., "Transpiration and Film Cooling Boundary Layer Computer Program--Vol. 1, Numerical Solutions of the Turbulent Boundary Layer Equations with Equilibrium Chemistry, NAS7-791, Prepared by Dynamics Science, Irvine, California, June, 1971.

8. Cohen, H., Rogers, G. F. C., and Saravanamuttoo, H. J. H., Gas Turbine Theory, 2nd ed., Longman, London, 1974, pp. 205-221.

9. Jacobs, E. N., Ward, K. E., and Pinkerton, R. M., "The Characteristics of 78 Related Airfoil Sections From Tests in the Variable-Density Wind Tunnel," NACA Report No. 460, 1933.

10. Ainley, D. G., "Performance of Axial Flow Turbines," Internal Combustion Turbines, ASME, 1949.

11. Dubberley, D. J., "An Analytical Parameter Study on the Erosion of Turbine Blades Subjected to Flow Containing Particulates," MS Thesis, Virginia Polytechnic Institute and State University, July, 1977.

12. Schlicting, H., Boundary Layer Theory, 6th ed., McGraw-Hill, New York, 1968, pp. 523-539.

13. Crank, J., and Nicolson, P., "A Practical Method for Numerical Evaluation of Solutions of Partial Differential Equations of the Heat Conduction Type," Proc. of the Cambridge Phil. Soc., Vol. 43, 1947, p. 50.

14. Flügge-Lotz, J., and Blottner, F. G., Tech. Report No. 131, Division of Engineering Mechanics, Stanford University, California, 1962.

15. Clausing, A. M., "Finite Difference Solutions of the Boundary Layer Equations," NASA CR-108909, Prepared by University of Illinois at Urbana-Champaign, Feb. 1970.

16. Pierce, F. J., and Klinksiek, W. F., "An Implicit Numerical Solution of the Turbulent Three-Dimensional Incompressible Boundary Layer Equations," Int. Tech. Report No. 3, ARO-D Project No. 6858E, Contract DAH C04 67 C 008, Prepared by Virginia Polytechnic Institute and State University, July, 1971.

17. Moses, H. L., "The Behavior of Turbulent Boundary Layers in Adverse Pressure Gradients," MIT Gas Turbine Laboratory Report No. 73, Jan., 1964.

18. Katsanis, T., "Computer Program for Calculating Velocities and Streamlines on a Blade-to-Blade Surface of a Turbomachine," NASA TN D-4525, Lewis Research Center, 1969.

19. Ahlberg, J. H., Nilson, E. N., and Walsh, J. L., The Theory of Splines and Their Application, Academic Press, New York, 1967.

20. Cebeci, T., "Calculation of Compressible Turbulent Boundary Layers with Heat and Mass Transfer," AIAA Paper No. 70-741, 1970.

21. White, F. M., Viscous Fluid Flow, McGraw-Hill, New York, 1974, pp. 273-280.

Appendix: The Crank-Nicolson Computer Code

The calculations were performed on an IBM 370-158 electronic digital computer maintained by the Virginia Tech Computing Center. The finite difference algorithm is written in a form suitable for use with the FORTRAN H compiler. Typical execution time for the algorithm is 0.005 CPU seconds per node.

The computer code is constructed of subroutines to aid the later user in applying and understanding the algorithm. Figure A1 shows the structure of the code. The following list is a description of the operations performed by the various subroutines.

CALCCF Subroutine CALCCF calculates the third and fourth coefficients (C(3,I) and C(4,I)) in the piecewise cubic spline fit to C(1,I) utilizing the tri-diagonal character of the matrix of coefficients.

CONTIN Subroutine CONTIN solves the equation governing conservation of mass in the boundary layer.

EDVISC Subroutine EDVISC contains the eddy viscosity model. For the laminar calculations, the eddy viscosity is "turned off" with $\varepsilon=0$.

INPUTS Subroutine INPUTS accepts all data read into the code. INPUTS also performs the spline fit to the edge velocity distribution as well as setting up the initial velocity profiles.

MAIN The program MAIN controls the flow of logic for the Crank-Nicolson implicit finite difference algorithm.

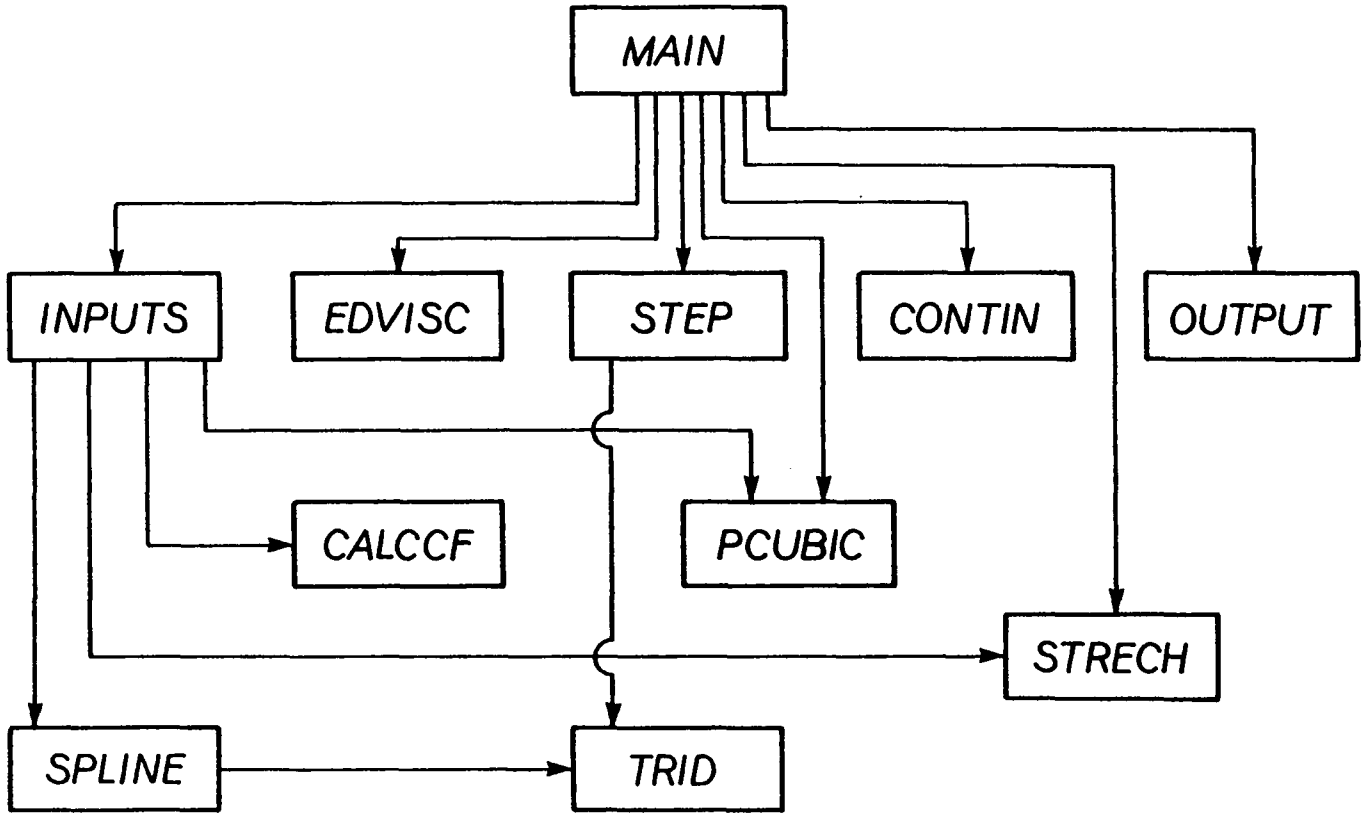

Fig. A1 Flow Chart for Crank-Nicolson Algorithm

OUTPUT Subroutine OUTPUT calculates the boundary layer characteristics using trapezoidal integration in the dimensionless plane. OUTPUT also writes all output data.

PCUBIC Subroutine PCUBIC evaluates the spline interpolating polynomial and its first derivative.

SPLINE Subroutine SPLINE calculates the second coefficient (C(2,I)) in the piecewise cubic spline fit to C(1,I). SPLINE is written for the "free end" condition, i.e., the second derivative of the spline polynomial is zero at the extreme points.

STEP Subroutine STEP solves the equation of conservation of momentum in the boundary layer by calculating the tri-diagonal matrix of coefficients and calling the tri-diagonal algorithm.

STRECH Function STRECH contains the coordinate transformation for the transverse direction. For the laminar calculations, the stretching function is reduced to $y = G(\tilde{y}) = \tilde{y}$.

TRID Subroutine TRID solves a system of algebraic equations whose matrix of coefficients is tri-diagonal.

The vita has been removed from the scanned document

A FINITE DIFFERENCE SOLUTION TO THE TWO-DIMENSIONAL WALL JET ON A COMBUSTION TURBINE BLADE

by

Martin David Harsh III

(ABSTRACT)

A simple model for the interaction of a tangentially oriented wall jet with the boundary layer is presented. The boundary-layer equations for steady, two-dimensional, homogeneous, incompressible flow are solved using an implicit finite difference technique. Calculations are performed for laminar and turbulent boundary-layer flows with and without tangential jet injection. Results from the finite difference calculation for the laminar, non-injected cases are compared with the Falkner-Skan similarity solutions. Results from the finite difference calculation for the turbulent, non-injected cases are compared with a two-parameter integral analysis. The boundary-layer calculation is applied to wall-jet injection near the leading edge of a representative combustion turbine blade. The blade geometry is developed by distributing a standard airfoil section over a single-parabolic camber line.